

THESIS FOR THE DEGREE OF LICENTIATE OF ENGINEERING

**Stabilizing zinc metal anodes for rechargeable zinc-metal
batteries: from imaging to interface engineering**

Marita Afiandika

Department of Physics
CHALMERS UNIVERSITY OF TECHNOLOGY
Gothenburg, Sweden, 2025

Stabilizing zinc metal anodes for rechargeable zinc-metal batteries: from imaging to interface engineering

MARITA AFIANDIKA

© Marita Afiandika, 2025
except where otherwise stated.
All rights reserved.

Department of Physics
Division of Material Physics
SE-412 96 Göteborg,
Sweden
Phone: +46(0)31 772 1000

Cover:

Rechargeable zinc-metal batteries: X-ray tomography as a characterization tool and interface engineering strategies for long cycle life.

Printed by Chalmers Digitaltryck,
Gothenburg, Sweden 2025.

Stabilizing zinc metal anodes for rechargeable zinc-metal batteries: from imaging to interface engineering

MARITA AFIANDIKA

*Department of Physics
Chalmers University of Technology*

Abstract

Ongoing trends in electrification and digitalization have pushed forward the diversification of energy storage systems, particularly rechargeable batteries, to meet the demands of various applications. To date, lithium-ion batteries remain the leading technology on the battery market, especially for electric vehicles. However, no single battery chemistry is suitable for all use cases, which emphasizes the importance of developing complementary battery technologies. Rechargeable zinc batteries, particularly with zinc metal anodes, have been suggested as an alternative solution due to cost, safety and sustainability aspects. However, inhomogeneous Zn deposition and side reactions on the zinc anodes continue to be major obstacles for the long-term stability of rechargeable Zn-metal batteries.

The cycle life of Zn-metal batteries can be extended by regulating Zn deposition and addressing interfacial issues on the Zn anode. In this thesis, the fundamental mechanisms of Zn deposition and dissolution have been investigated through real-time X-ray tomographic imaging, design of a functional cellulose-based separator and optimisation of the electrolyte formulation. From X-ray tomography we show how we can follow the deposition and stripping processes on the metal anode in real time and that we can quantitatively correlate the volume change of Zn during deposition and stripping and the Coulombic efficiency obtained from electrochemistry recorded simultaneously. To improve the processes at the metal anode interface we have also investigated the role of a functional cellulose-based separator, built up of (TEMPO)-oxidized cellulose nanofibrils and cellulose nanocrystals, as well as the role of changing the solvation structure of Zn ions in the electrolyte by a low-transition-temperature Zn(TFSI)₂ and ethylene glycol electrolyte formulation.

Keywords: metal anodes, zinc, stripping, deposition, imaging, separator, electrolyte

List of Papers

This thesis is based on the studies from the papers listed below:

Paper 1: *Operando* 3D visualization of zinc plating and stripping by X-ray tomographic microscopy

Marita Afiandika, Josef Rizell, Matteo Palluzzi, Matthew Sadd, Federica Marone, Shizhao Xiong, Aleksandar Matic

In manuscript

Paper 2: Physicochemical and electrochemical characterization of hybrid cellulose separators for aqueous zinc-ion batteries

Marita Afiandika, Aleks Zitting, Amit Kumar Sonker, Shizhao Xiong, Gunnar Westman, Aleksandar Matic

In manuscript

Paper 3: A low-transition-temperature electrolyte based on ethylene glycol for rechargeable zinc-ion batteries

Matteo Palluzzi, Marita Afiandika, Shizhao Xiong, Akiko Tsurumaki, Paola D'Angelo, Aleksandar Matic, Maria Assunta Navarra

Electrochimica Acta, 525 (2025): 146061

Contribution Report

Paper 1:

SX proposed the synchrotron tomography experiment. MA and SX planned the experiments with input from JR, MS, and AM. MA, JR, MP, MS, FM, and AM performed the synchrotron experiment. MA performed all data analyses, wrote the first draft of the manuscript, and finalized the paper with co-authors.

Paper 2:

MA, AK, SX, and GW planned the experiments. AK prepared the TCNF, GW prepared the CNC, and MA prepared the cellulose separators. MA performed all sample characterization and electrochemical experiments, except for SAXS-WAXS. AZ and MA performed SAXS-WAXS measurements. MA analyzed all data, except for SAXS-WAXS, and wrote the first draft of the manuscript, except for the SAXS-WAXS section. AM supervised MA, managed project conceptualization, administration, and resources, and reviewed and edited the manuscript.

Paper 3:

MP planned and carried out the experiments with input from SX, AT, PD, AM, and MAN. MA prepared the aqueous electrolyte and cathode materials and performed the electrochemical measurement for the full cell assembly. MA participated in the discussion, preparation, and revision of the manuscript.

Publications Not Included in This Thesis

Acid-Treatment-Assisted Liquid Metal–Based Zinc Metal Anode for Stable Aqueous Zinc-Ion Batteries

Hyungsub Yoon, Chunghyeon Choi, Seungwoo Hong, Marita Afiandika, Aleksandar Matic, Tae Gwang Yun, Byungil Hwang

International Journal of Energy Research, 2025, 1405163

Understanding the electro-chemo-mechanics of lithium metal anodes

Quan Wu, Elin Dufvenius Esping, Marita Afiandika, Shizhao Xiong, Aleksandar Matic

eScience, 2025, 100429

Contents

Abstract	i
List of Papers	iii
Contribution Report	iv
Publications Not Included in This Thesis	v
1 Introduction	1
2 Rechargeable Zinc-Metal Batteries	3
2.1 Working principle of rechargeable zinc-metal batteries	4
2.2 Zinc metal anodes	4
2.3 Electrodeposition of zinc	5
2.4 Zinc nucleation and growth	6
2.5 Challenges of zinc metal anodes	8
2.5.1 Hydrogen evolution reaction	9
2.5.2 Corrosion and passivation	11
2.5.3 Non-uniform deposition morphology	12
2.6 Electrolyte development	14
3 Experimental and Theory	17
3.1 Preparation of electrolytes, electrode, and cellulose separator .	17
3.1.1 Standard electrolyte (2 M ZnSO ₄)	17
3.1.2 Low-transition-temperature electrolyte	17
3.1.3 KVO electrode	17
3.1.4 Cellulose separators	17
3.2 Electrolyte uptake	18
3.3 Electrochemical experiments	18

3.3.1	Electrochemical cells	18
3.3.2	Electrochemical impedance spectroscopy	19
3.3.3	Linear sweep voltammetry	19
3.3.4	Galvanostatic cycling	21
3.4	Imaging techniques	23
3.4.1	<i>Operando</i> synchrotron X-ray tomographic microscopy .	24
3.4.2	Scanning electron microscopy	26
3.5	Vibrational spectroscopy	28
4	Results and Discussion	31
4.1	Mechanisms of Zn deposition and stripping	31
4.2	Separator design	33
4.3	Electrolyte engineering	36
5	Conclusions and Outlooks	39
	Acknowledgements	41
	References	52

Chapter 1

Introduction

In the 21st Century, the shift from fossil fuel-based transportation to electric vehicles is accelerating as part of global efforts for decarbonization [1]. Beyond transportation, the rapid expansion of the Internet of Things (IoT) in applications such as smart homes, cities, and healthcare necessitates batteries to power a diverse range of small devices [2]. On a larger scale, grid applications demand batteries capable of storing energy from renewable sources, ensuring efficient storage and reliable future utilization of this energy [3].

Lithium-ion batteries currently dominate the market due to their high energy density and long cycle life [4]. However, they face sustainability challenges from both socioeconomic and environmental aspects [5]. One significant issue relates to the extraction of raw materials such as lithium, cobalt, and nickel, which impose substantial ecological burdens, while geopolitical risks in the supply chain threaten long-term availability [5], [6]. Safety is another critical concern, as Li-ion batteries can present fire and toxicity hazards in the event of thermal runaway [7], [8].

No single battery technology can meet all the criteria of the diverse landscape of electrochemical energy storage. Therefore, it is essential to consider how various applications impose different demands on battery performance. While Li-ion batteries will retain their role for high energy density applications, such as electric vehicles, other sectors have different priorities [9]. For example, IoT devices, which can operate at cell voltages of 1.2-1.5 V, do not require the high voltage or energy density of Li-ion batteries [10]. Grid-scale prioritizes affordability, low environmental footprint, long cycle life, high power, and high energy efficiency [10], [11].

The diversity in requirements highlight the need for alternative and sustainable battery chemistries that meet growing demand while delivering longer lifetime, faster charging, enhanced safety, greater affordability, and minimal environmental impact [12], [13]. Potential candidates include rechargeable batteries based on monovalent metal ions, such as sodium (Na^+) and potassium (K^+) [14], or multivalent ions, such as calcium (Ca^{2+}), magnesium (Mg^{2+}), zinc (Zn^{2+}), and aluminium (Al^{3+}) [15]. Among these options, multivalent ions are particularly promising because they can transfer more electrons per ion in the redox process, potentially increasing volumetric

energy density [16], [17].

Among multivalent battery chemistries, rechargeable Zn-metal batteries offer several advantages, including a low toxicity, low raw material costs [18], [19], and greater abundance of zinc in the Earth's crust compared to lithium [20]. In addition, rechargeable Zn-metal batteries with aqueous electrolytes allow for simpler processing and manufacturing, as they require no specialized atmosphere with controlled moisture and oxygen content [21], [22]. The use of aqueous electrolytes also improves safety aspects by eliminating fire or explosion risks, reducing the need for complex safety systems [23].

Nevertheless, despite these advantages, rechargeable Zn-metal batteries face challenges at the electrode-electrolyte interface that must be overcome before commercialization. Uneven deposition arises from the preferential growth of Zn in areas with higher local current density [24]. Meanwhile, side reactions occur due to the reactivity of water molecules in the electrolyte, leading to hydrogen evolution, Zn corrosion, and passivation. These processes decrease the reversibility of the Zn anode and reduce cycling stability [25], [26]. Addressing these interfacial issues, particularly the uneven Zn deposition, requires a thorough understanding of the processes that occur during cycling. Real-time characterization is therefore essential, as it allows direct observation of changes on the electrode during cycling [27] and provides mechanistic insights to guide the design of more durable rechargeable Zn-metal batteries.

This thesis focuses on understanding the mechanisms of Zn deposition and dissolution in aqueous electrolytes and investigating interfacial engineering strategies, such as electrolyte and separator design, to enhance the stability of Zn-metal anodes. Full cell data of Zn||KVO is presented, however, cathode development and related storage mechanisms are outside the scope of this work. In Paper 1, X-ray tomography is applied to study the growth and dissolution mechanisms of Zn in an aqueous electrolyte during cycling. Building on these findings, Paper 2 presents a functional hybrid cellulose separator that can suppress the harmful growth morphology of Zn, while Paper 3 presents an electrolyte design that extends cycling stability by reducing water-induced side reactions. These studies provide a combined approach of advanced synchrotron X-ray imaging with interface engineering to overcome the instability of the Zn anode.

Chapter 2

Rechargeable Zinc-Metal Batteries

This chapter begins by introducing how a metal battery operates and outlining the basic processes of charging and discharging. The discussion then narrows to the Zn-metal anode, first examining its electrochemical behavior in both alkaline and acidic electrolytes. The chapter then explores the mechanisms of zinc electrodeposition, including nucleation and growth. Finally, it addresses the problems of Zn-metal anodes and electrolyte development for rechargeable Zn-metal batteries.

Before delving into these topics, it is important to clarify the terminology used in literature to describe rechargeable Zn-metal batteries. They are most commonly referred to as zinc-metal batteries or zinc-ion batteries. The former refers exclusively to systems that use metallic Zn as the anode, whereas the latter may employ either Zn-metal or Zn-intercalating anodes (e.g., Mo_6S_8 and $\text{Na}_{0.14}\text{TiS}_2$) [28]. In this thesis, for simplicity, the term rechargeable Zn-metal batteries will be used to denote all systems utilizing Zn-metal anodes. Additionally, some authors refer to the anode as the negative electrode during discharge and the cathode as the negative electrode during charge in rechargeable batteries [29]. To ensure clarity, this thesis will consistently use the term Zn-metal anode.

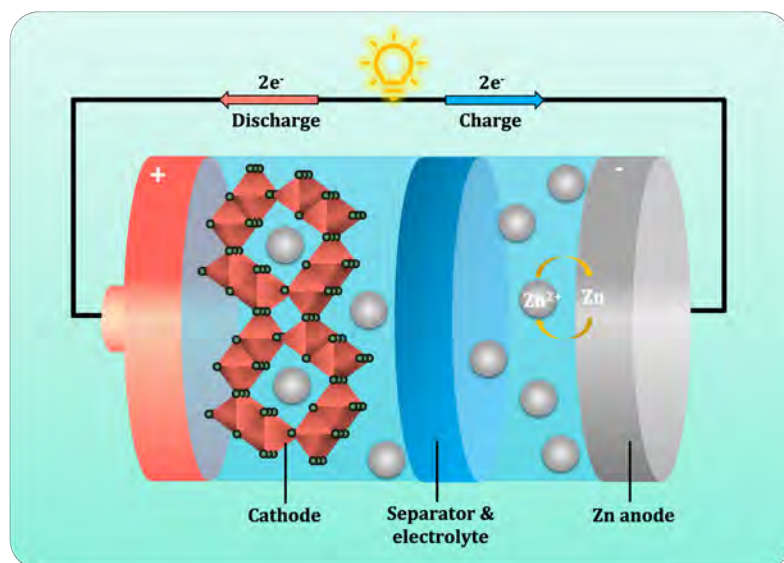


Figure 2.1: Schematic illustration of the working principle of a rechargeable Zn-metal battery.

2.1 Working principle of rechargeable zinc-metal batteries

Figure 2.1 illustrates a typical rechargeable Zn-metal battery that comprises a Zn-metal anode, an intercalation-type cathode (e.g., MnO_2 or V_2O_5), a separator, and an electrolyte. During discharge, when the cell is connected to an external load, electrons flow from the anode to the cathode (with current flowing in the opposite direction). Charging reverses the processes, and the repetition of these reversible reactions defines the battery life cycle, typically considered to end when the discharge capacity falls below 80% of its initial value [30].

Specifically for Zn metal anodes and as in other metal batteries, the electrode undergoes redox reactions: during charging, Zn is deposited onto the anode surface, whereas during discharging it dissolves back into the electrolyte [31]. These processes are often referred to as plating and stripping. However, for consistency, this thesis will use the terms deposition and stripping.

2.2 Zinc metal anodes

Metallic zinc has played a key role in battery technology for a long time, starting with the copper–zinc battery invented by Daniell in 1836 [32]. Zinc electrodes were initially used in primary batteries such as zinc–air, zinc–manganese, zinc–nickel, and zinc–silver oxide batteries. In 1986, a Zn/ MnO_2 chemistry using an aqueous ZnSO_4 electrolyte was developed [33], but gained little attention due to unclear redox mechanisms. In 2009, Kang et al. demonstrated reversible Zn^{2+} intercalation in MnO_2 ($\text{Zn} + 2\text{e}^- + 2\text{MnO}_2 \rightleftharpoons \text{ZnMn}_2\text{O}_4$) and later introduced the concept of “zinc-ion batteries (ZIBs)” in 2011 [34].

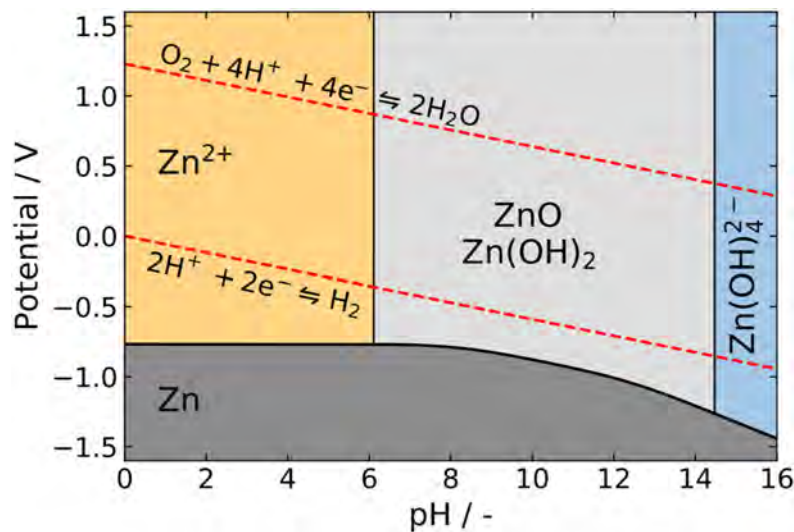
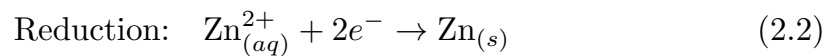
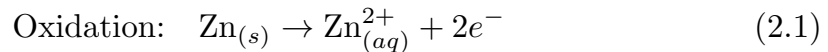


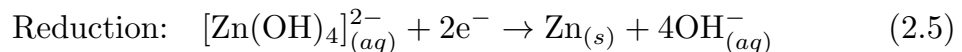
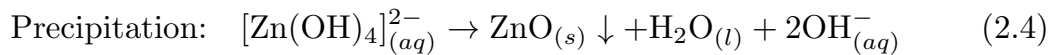
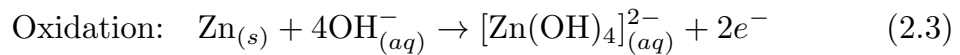
Figure 2.2: Pourbaix diagram of Zn in aqueous electrolytes with different pH. Reprinted from Brochers et al. [35], Copyright 2021, with permission from Elsevier.

To understand how rechargeable Zn batteries operate in different aqueous electrolytes, it is essential to first consider the electrochemical behavior of Zn as a function of pH. Figure 2.2 illustrates the various Zn species and their stability across a wide pH range. As seen in the Pourbaix diagram, Zn is stable as Zn^{2+} in acidic electrolytes, whereas zincate and ZnO dominate in alkaline electrolytes. These stability regions determine the electrochemical reactions in acidic and alkaline electrolytes, as outlined below.

In acidic electrolytes, the electrochemical reactions at the Zn metal anode are more straight forward (Eq. (2.1) and (2.2)), as summarized by the following reactions [36]:



In contrast, the electrochemistry at the Zn-metal anode is rather complex in alkaline electrolytes. During discharge, the Zn-metal anode reacts with hydroxide ions (OH^{-}) to form zincate ($[\text{Zn}(\text{OH})_4]^{2-}$) (Eq. (2.3)). The high concentration of zincate causes the formation of zinc oxide (ZnO) (Eq. 2.4) once the saturation limit has been reached. The ZnO passivates the metal surface, reducing active material utilization [28]. Upon charging, zinc deposition occurs through the reduction of zincate (Eq. 2.5).



While these equations describe the fundamental redox reactions, the actual reversibility of rechargeable Zn-metal batteries depends on how Zn dissolves and deposits at the Zn anode. To better understand this process, we now turn to the electrodeposition mechanisms.

2.3 Electrodeposition of zinc

In metal batteries, unlike ion batteries, the active material is stored directly on the anode surface through metal deposition rather than intercalation into a host material. Figure 2.3 illustrates the steps involved in Zn electrodeposition in alkaline and acidic electrolytes, which proceed through mass transfer, desolvation, charge transfer, and nucleation/electrocrystallization [37].

In the electrolyte, Zn^{2+} exists as solvent-coordinated Zn^{2+} , such as zinc hexaaqua ($[\text{Zn}(\text{H}_2\text{O})_6]^{2+}$) in acidic and zinc tetrahydroxyzincate ($[\text{Zn}(\text{OH})_4]^{2-}$) in alkaline electrolytes. Under an applied electric field, these solvated ions move

in the bulk electrolyte toward the Zn anode surface (mass transfer). At the surface, desolvation occurs, where the solvated ions release the ligand/solvent molecules to form Zn^{2+} [37], [38]. Subsequently, the Zn^{2+} picks up electrons at the interface and forms adsorbed Zn on the electrode surface (charge transfer). Adsorbed Zn atoms either nucleate and grow, or they will diffuse to the proper location (growth point) along the electrode surface and enter the metal lattice [37]. This step determines the morphology of the Zn deposits. In addition, both the Zn^{2+} solvation shell and the anode surface condition critically affect the homogeneity of the deposition morphology of Zn [37].

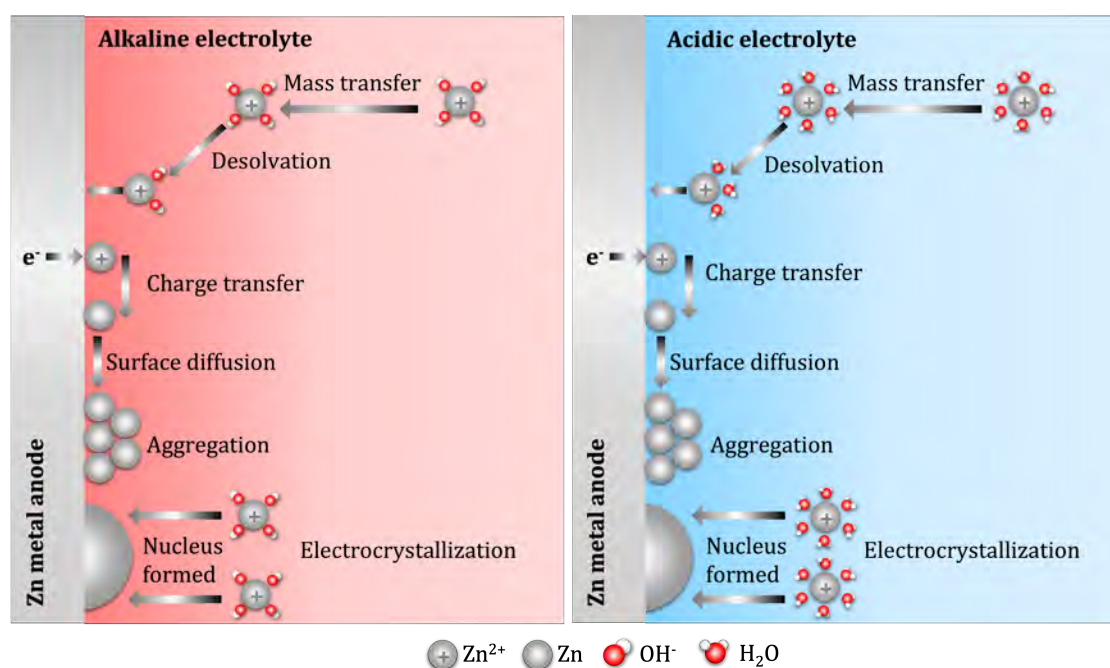


Figure 2.3: Schematic of Zn electrodeposition in alkaline (left) and acidic (right) electrolytes. Adapted from Ref. [38] (Copyright 2024, Royal Society of Chemistry), under Creative Commons license.

2.4 Zinc nucleation and growth

To nucleate and form metallic Zn, Zn ions must overcome a nucleation overpotential, which is influenced by desolvation of metal ions [39], electrode roughness, electric field distribution, and substrate zincophilicity [40]. In practice, electrode surfaces are rarely atomically smooth, leading to uneven local electric field, variations in surface energy, and site-dependent nucleation barriers [41], [42]. Once initial Zn deposits form, surface irregularities amplify the local electric field, particularly at convex regions or tips. This “tip effect” lowers the nucleation barrier at these sites, promoting preferential Zn reduction and nonuniform growth [43]. Hence, to guarantee uniform nucleation and growth, the interfacial electric field must be homogeneous to ensure cycle

stability [44].

After nucleation, growth begins, which is also governed by the substrate's zincophilicity. Substrates with higher zincophilicity, that have strong Zn bonding ability, promote uniform ion attachment, and direct the development of smooth and continuous Zn deposits, thereby suppressing uneven growth [45], [46]. Zn deposits can be classified according to (i) the shape of individual Zn particles and (ii) the orientation of Zn plates. The first aspect often refers to plate-like morphologies, since hexagonal close-packed Zn crystals preferentially expose the (002) plane in aqueous electrolytes [47]. The second aspect describes the alignment of Zn plates, which may be random, parallel, or vertical [47]. However, no standardized terminology currently exists for describing the morphologies of Zn deposits.

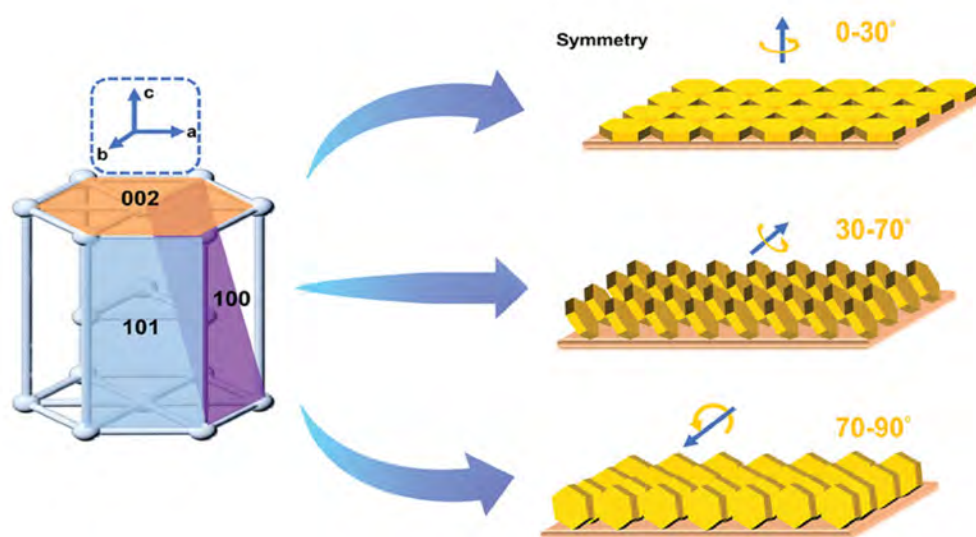


Figure 2.4: Illustration of hexagonal closed-pack Zn with different crystal plane orientations. Reprinted with permission from Tian et al. [48] (Copyright 2024, John Wiley & Sons).

Since Zn is a crystalline material, the crystal orientation determines the growth pattern. When deposition favors the Zn (100) and (101) planes, Zn tends to grow at a large angle (30° – 90° to the substrate), forming nanosheet structures. In contrast, preferential exposure of the Zn (002) plane leads to growth at a small angle (0° – 30°), resulting in horizontal deposition [48], [49] (Figure 2.4). Among possible orientations, the Zn (002) plane is considered the most desirable for achieving stable and reversible Zn deposition, as it promotes lateral growth, smooth and dense deposits, resistance to side reactions, and suppression of dendrite formation [48].

Nucleation and growth are also strongly influenced by applied current density [50]. At low current densities ($< 1 \text{ mA cm}^{-2}$), the deposits are commonly

hexagonal Zn nanosheets. When the current density is increased to 10 mA cm^{-1} , the Zn deposits become dense and spherical. Further increase of the current density to $> 100 \text{ mA cm}^{-2}$, non-uniform tree-like deposits have been observed [51]. It should be noted that the separator microstructure also affects the Zn deposition morphology [52]. For example, porous separators like glass fiber can trap Zn within their pores, leading to inactive Zn after stripping, whereas nonporous separators block dendrite penetration [52].

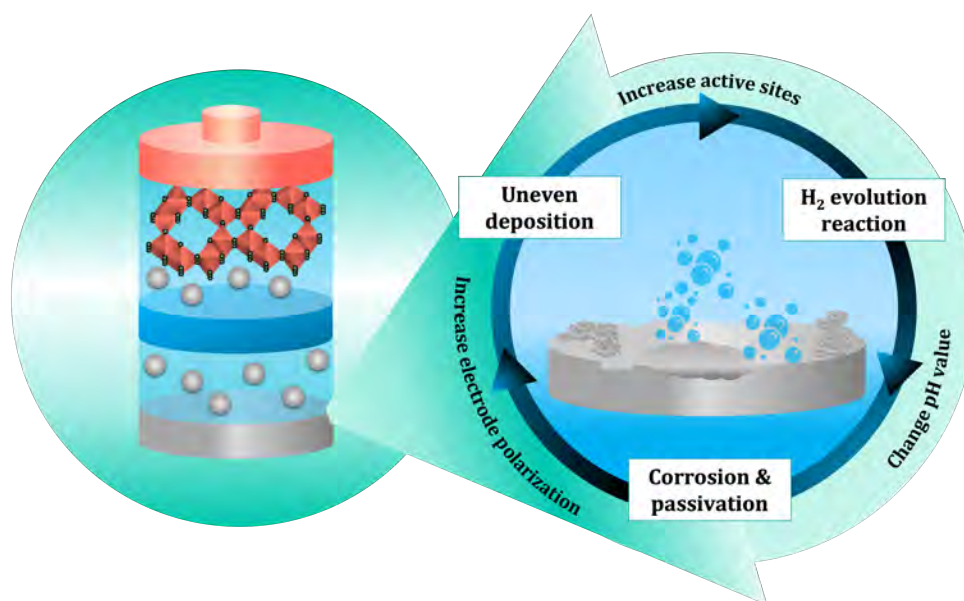


Figure 2.5: Illustrations of issues on Zn-metal anode in aqueous rechargeable Zn-metal batteries and their relationship.

2.5 Challenges of zinc metal anodes

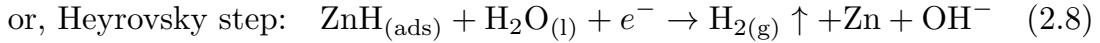
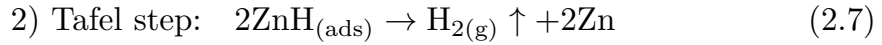
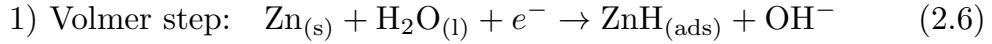
The Zn metal anode faces multiple interfacial issues at the electrode-electrolyte interface in aqueous electrolytes, including hydrogen evolution, corrosion, passivation, and uneven zinc deposition, which are closely related as shown in Figure 2.5.

Inhomogeneous Zn deposition accelerates the hydrogen evolution reaction, which increases the pH of the electrolyte due to the local accumulation of OH^- at the Zn anode–electrolyte interface. This leads to electrochemical corrosion and the formation of corrosion by-products. When the concentration of these by-products in the electrolyte reaches the solubility limit, they deposit on the anode surface, further promoting uneven Zn deposition [53], [54], [55]. The following sections delve into these issues in more detail.

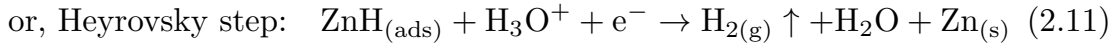
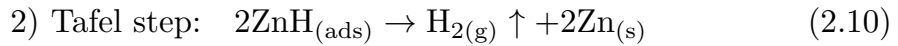
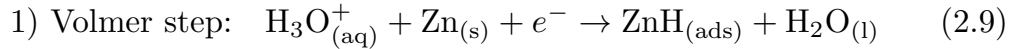
2.5.1 Hydrogen evolution reaction

The hydrogen evolution reaction negatively impacts rechargeable Zn-metal batteries by competing with the reduction of Zn^{2+} . The Pourbaix diagram (Figure 2.2, section 2.2) shows that the equilibrium potential of H^+/H_2 is higher than Zn^{2+}/Zn in the whole pH region, implying that hydrogen gas evolution is thermodynamically more favourable compared to Zn electrodeposition. This side reaction consumes electrons and zinc, reducing Zn utilization and thereby lowering Coulombic efficiency. In addition, the buildup of H_2 gas increases internal pressure, which can lead to battery swelling. The hydrogen evolution reaction also alters the local pH, promoting the formation of corrosive byproducts [56]. This latter effect will be discussed in more detail in section 2.5.2.

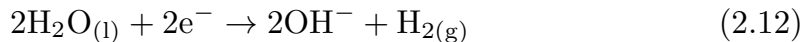
The steps of the hydrogen evolution reaction differs depending on the pH of the electrolyte [57] and involves two steps: 1) the Volmer step and 2) the Heyrovsky step or the Tafel step [40]. In alkaline electrolytes, the hydrogen evolution reaction proceeds according to:



Compared to the hydrogen evolution reaction in alkaline electrolytes, the Volmer and Heyrovsky steps in acidic electrolytes involve hydronium ions (H_3O^+), while the Tafel step remains unchanged. The steps of the hydrogen evolution reaction in acidic electrolytes are:



The hydrogen evolution reaction can also occur due to the dissociation of water. The thermodynamic stability of water depends on the O–H bond strength, with stronger bonds making water more stable. However, intermolecular hydrogen bonding weakens the O–H bond and lowers the barrier for water dissociation, leading to the generation of hydrogen gas [58] according to



Zn deposition can still dominate over hydrogen evolution due to the slower kinetics of the hydrogen evolution reaction [43]. The hydrogen evolution reaction is strongly influenced by the electrochemical overpotential, which is determined by the binding strength between the adsorbed hydrogen intermediate (H_{ads}) and the Zn surface. Both very weak and very strong binding can suppress hydrogen evolution: weak binding prevents protons from adsorbing onto the Zn surface, while strong binding limits the release of hydrogen gas through the Tafel process. In the case of Zn, the Zn- H_{ads} bond is relatively weak, giving metallic Zn a comparatively high hydrogen evolution overpotential [58].

The current density also affects the overpotential of the hydrogen evolution reaction. Experimental results show that hydrogen evolution occurs at potentials ranging from -1.08 to -1.54 V vs. Ag/AgCl, which are more negative than those for Zn deposition (-1.02 to -1.12 V vs. Ag/AgCl) across a range of current densities ($0.1 - 5.0 \text{ mA cm}^{-2}$) in various 2 M electrolytes: 2 M ZnSO_4 , 2 M $\text{Zn}(\text{OTf})_2$, and 2 M ZnCl_2 [59].

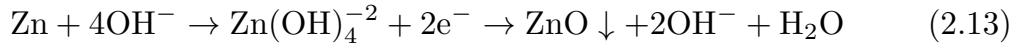
Alloying Zn metal with tin (Sn) and bismuth (Bi) has been shown to inhibit H_2 formation. These metals increase the hydrogen evolution reaction overpotential by altering the hydrogen adsorption behavior [60], [61]. Density functional theory calculations indicate that Bi and Sn exhibit high Gibbs free energy differences of H adsorption ((ΔG_{H}^*)), meaning hydrogen evolution requires a higher activation overpotential. By contrast, transition metals such as Co and Ni can catalyze the hydrogen evolution reaction, thereby lowering the overpotential [62]. Typically, linear sweep voltammetry is employed to determine the cathodic onset potential at which the hydrogen evolution begins [63].

Recently, surface engineering approaches have also been proposed to inhibit hydrogen evolution. For example, 2D transition metal carbide [64] made of Nb_2C , denoted $\text{Nb}_2\text{C}@\text{Znp}$, was applied to coat a $50 \text{ }\mu\text{m}$ -thick Zn foil ($\text{Nb}_2\text{C}@\text{Znp} - \text{Zn}$) [65]. The strategy relies on regulating the M- H^* bond and first principle calculations show that a monolayer of Nb_2C forms a relatively weak M - H^* bond, which reduces H^* adsorption. This blocks the rate-limiting Volmer step, thereby suppressing subsequent Tafel or Heyrovsky steps. Electrochemical evaluation confirmed this effect. At 4 mA cm^{-2} , the hydrogen evolution potential of $\text{Nb}_2\text{C}@\text{Znp} - \text{Zn}$ electrodes reached 1.97 V vs. RHE, which is 0.51 V higher than for bare Zn (1.46 V vs. RHE). This result clearly demonstrates that the $\text{Nb}_2\text{C}@\text{Znp}$ layer effectively suppresses hydrogen evolution [65].

2.5.2 Corrosion and passivation

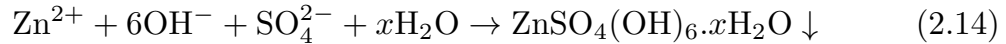
Two other issues that impact the lifespan of rechargeable Zn-metal batteries are corrosion and passivation of the Zn anode. These phenomena are influenced by the electrolyte pH and can be classified as chemical or electrochemical corrosion [66]. With respect to electrochemical corrosion, it is related to hydrogen evolution [66], which has been discussed in subsection 2.5.1.

The chemical corrosion in alkaline electrolytes can be expressed as [67]:



The low thermodynamic stability of soluble $\text{Zn}(\text{OH})_4^{2-}$ eventually leads to the formation of ZnO on the metal anode, resulting in chemical corrosion [53]. This increases the internal resistance of the battery and surface roughness [68].

In contrast, in acidic electrolytes containing ZnSO_4 , for example, water decomposition and H^+ consumption lead to OH^- enrichment at the electrode surface. This OH^- can react with SO_4^{2-} , forming an insoluble by-product [67]:



Depending on the Zn salt used, in the acidic electrolyte different corrosion by-products are formed. For instance, in acidic electrolytes with $\text{Zn}(\text{NO}_3)_2$ and $\text{Zn}(\text{CH}_3\text{CO}_2)_2$, the corrosion products have been reported to be $\text{Zn}_5(\text{OH})_8(\text{NO}_3)_2 \cdot 2\text{H}_2\text{O}$ and $\text{Zn}_5(\text{OH})_6(\text{CO}_3)_2$, respectively [69].

Notably, these corrosion byproducts typically exhibit poor electrical conductivity and limited solubility in the electrolyte and ultimately passivate the Zn anode, hindering further electrochemical reactions to take place [53], [67], [70]. The corrosion reaction also leads to Zn consumption and capacity fade [68]. Additionally, the rough surface morphology induced by the accumulation of by-products on the anode surface will promote the growth of Zn dendrites, further compromising battery performance [68].

To address the issues of corrosion and passivation, a liquid-metal coating of eutectic gallium–indium (EGaIn–LM@AZn) has been applied to the Zn anode surface to improve both corrosion resistance and suppresses hydrogen evolution [71]. Since Ga–In alloys are essentially insoluble in aqueous electrolytes, the coating remains stable on the Zn anode. Furthermore, the EGaIn–LM layer suppresses corrosion and passivation caused by hydrogen evolution reaction, owing to the high overpotentials of Ga (Ga^{3+}/Ga : -0.53 V vs. SHE) and In (In^{3+}/In : -0.34 V vs. SHE). As a result, the coating increases the corrosion overpotential (Figure 2.6a) and reduces the formation of $\text{ZnSO}_4(\text{OH})_6 \cdot x\text{H}_2\text{O}$ deposits (Figure 2.6b). However, achieving uniform coating is difficult because

Zn has poor wettability toward liquid metals. Acid treatment of Zn metal anodes improves the surface wettability, enabling the formation of a homogeneous liquid-metal coverage [71], [72].

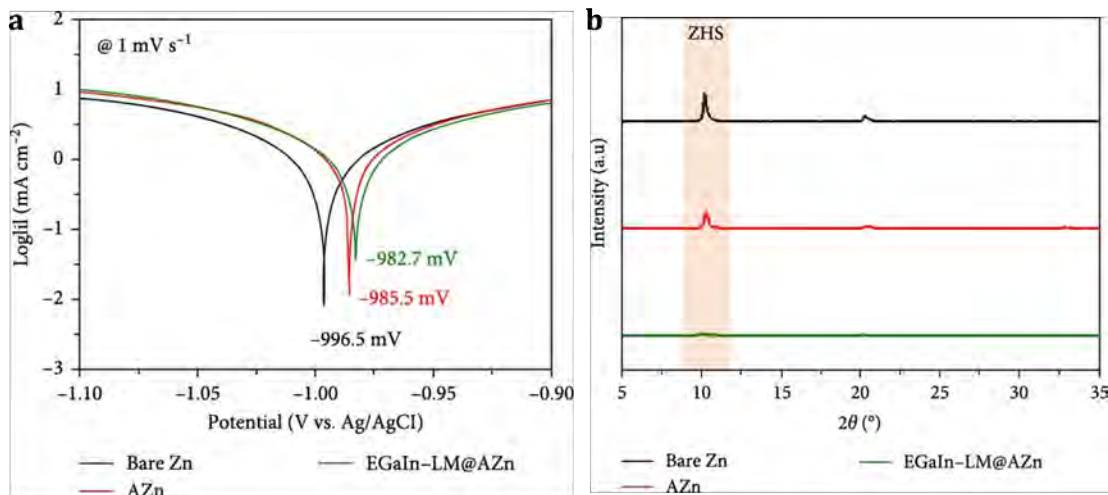


Figure 2.6: (a) Tafel plots from symmetric cells with bare Zn, acid treated Zn foil (AZn) and liquid metal coated acid treated Zn foil (EGaIn-LM@AZn). (b) XRD spectra after soaking electrodes (bare Zn foil, acid treated Zn foil and liquid metal coated acid treated Zn foil) for 10 days in 2 M ZnSO_4 aqueous electrolyte. Reproduced from Yoon et al. [71] (Copyright 2025, John Wiley & Sons), under Creative Commons Attribution License.

Side reactions can also be mitigated by introducing a strong Brønsted acid, such as bis(trifluoromethanesulfonyl)imide (HTFSI), into the conventional 1 M ZnSO_4 aqueous electrolyte, thereby modulating Zn corrosion pathways [73]. This shifts the corrosion potential from -0.99 to -0.97 V vs. Ag/AgCl and reduces the corrosion current density from 1.62 to 0.64 mA cm^{-2} , resulting in a lower corrosion tendency and rate. Introducing the strong Brønsted acid helps protect the Zn surface in several ways: (i) it maintains a relatively low pH at the Zn/electrolyte interface, which suppresses the formation and buildup of corrosion byproducts such as $\text{ZnSO}_4(\text{OH})_6 \times \text{H}_2\text{O}$; (ii) the bulky TFSI anions create a hydrophobic interfacial region depleted of free water molecules, thereby reducing direct Zn–water contact; and (iii) the presence of HTFSI promotes the formation of a ZnS-rich interphase (arising from SO_4^{2-} reduction), which further inhibits corrosion [73].

2.5.3 Non-uniform deposition morphology

The tendency of metals to form heterogeneous and rough electrodeposits poses a significant challenge for the implementation of metal anodes in general, not only Zn [74]. Although the exact mechanism remains unclear, key contributing factors include uneven local current density, ion depletion at the electrode

surface, and surface irregularities on the zinc electrode [75], [76].

During electrodeposition, the uneven electric field causes an uneven ion distribution, which promotes nucleation at sites with higher local current density [75], [76]. As a result, subsequent depositions take place on the existing deposits, causing morphological and uneven deposition [77]. These irregular deposits, particularly with sharp and needle-like morphology, as so-called "dendrite", can grow into the separator and bridge the cathode and anode, short-circuiting the cell and even causing explosion. Over extended cycling, the anode undergoes morphological changes that exacerbate side reactions and cause physical orphaning (loss of electrical contact of metal deposits) [78]. The loss of electrochemical connectivity leads to a decrease of active material on the electrode and, as a result, reduced efficiency and lifespan of the battery [78].

Controlling the morphological changes of Zn during cycling and enhancing reversibility are important for developing a high-performance Zn-metal anodes for low-cost batteries [78]. As discussed in Section 2.4, substrate zincophilicity strongly influences deposition uniformity. For example, coating the Zn anode with monolayer graphene, with a strong Zn binding energy (4.41 eV), results in a low nucleation overpotential and promotes uniform, planar Zn electrodeposition [79]. Similarly, graphene substrates have been shown to induce epitaxial Zn growth due to a low lattice mismatch with the Zn (002) [80].

Besides the Zn and substrate affinity, the electric field distribution on the anode surface also plays a critical role. Hong et al. demonstrated that an antimony (Sb) protective layer through an in situ replacement reaction reduced the local electric field strength on the electrode surface from 256.3 to 130.6 V m⁻¹, thereby making the electric field uniform. This facilitates homogeneous ion distribution and enabled dendrite-free Zn deposition [81].

An alternative route to achieve homogeneous deposition is through separator engineering. The use of separators with more homogeneous interface and with possibility for surface functionalization can provide a route to more homogeneous deposition [82], [83]. Nanocellulose-based separators are attractive since they can also add biodegradability, renewability, and lower end-of-life recycling [84]. Their abundant hydroxyl groups enhance electrolyte wettability, allowing for straightforward functionalization [85]. For instance, a cellulose nanofiber/MOF-derived C/Cu nanocomposite separator with a pore size of 3–20 nm has been shown to lower local current density, promote uniform Zn nucleation, and reduce charge-transfer resistance of zinc deposition [86]. Another strategy involves controlling the crystallographic orientation of Zn growth through the design of the separator. A graphene oxide–modified cellulose acetate separator, for instance, with low lattice mismatch between graphene

oxide and Zn, together with its oxygen-containing functional groups, was shown to promote uniform nucleation and epitaxial Zn growth along the (002) plane, thereby achieving dendrite-free deposition [87].

2.6 Electrolyte development

Research on rechargeable Zn-metal batteries has primarily focused on aqueous electrolytes due to their safety and low cost. Alkaline electrolytes, such as KOH, NaOH, and LiOH, are commonly used. However, they present challenges, as zinc dendrites and ZnO form more readily in strongly alkaline environments. By comparison, highly acidic electrolytes risk corroding the zinc anode and current collector. For this reason, neutral or mildly acidic aqueous electrolytes are generally preferred [88].

Mildly acidic electrolytes (pH 4–6) [89] are commonly formed by zinc salts dissolved in water. The salt can be, for instance, ZnCl_2 , $\text{Zn}(\text{NO}_3)_2$, $\text{Zn}(\text{ClO}_4)_2$, ZnF_2 , ZnI_2 , ZnSO_4 , ZnBr_2 , $\text{Zn}(\text{CH}_3\text{COO})_2$, $\text{Zn}(\text{CF}_3\text{SO}_3)_2$ or $\text{Zn}(\text{OTf})_2$, and $\text{Zn}(\text{CH}_3\text{CH}_2\text{SO}_3)_2$ or $\text{Zn}(\text{TFSI})_2$ [47], [90], [91]. Among these, ZnSO_4 salt is widely used for aqueous electrolytes in Zn-metal batteries due to low cost and compatibility with common cathode materials, e.g. V_2O_5 , in comparison with $\text{Zn}(\text{CH}_3\text{COO})_2$, $\text{Zn}(\text{NO}_3)_2$, and ZnCl_2 [92], [93].

The interactions between zinc ions, solvent molecules, anions, and additives directly determine the solvation structure of the Zn ions in the electrolyte. In liquid electrolytes, Zn ions are surrounded by solvent molecules, forming a primary solvation shell (e.g., $[\text{Zn}(\text{H}_2\text{O})_6]^{2+}$), which is stabilized by strong coordination and electrostatic interactions, and the Zn ions move together with this solvation shell in the electrolyte [94]. However, the bulky nature of $[\text{Zn}(\text{H}_2\text{O})_6]^{2+}$ often results in sluggish ion transport and slow desolvation at the electrode surface [95]. Therefore, tailoring solvation structures is essential for the design of electrolytes, and design strategies include, for instance, using highly concentrated electrolytes or incorporating organic solvents.

Highly concentrated electrolytes suppress the formation of $[\text{Zn}(\text{H}_2\text{O})_6]^{2+}$ since at the high salt concentration there are not enough solvent molecules (water) available to solvate the Zn ions and anions are introduced in the primary solvation shell. In addition, since there is less water molecules in the primary solvation shell, less water molecules are also present at the electrode surface and thus, less H_2 is formed [96]. A well-known example is a water-in-salt electrolyte composed of 1 m $\text{Zn}(\text{TFSI})_2$ + 20 m LiTFSI [97]. In this electrolyte, anions are also part of the solvation shell of Zn^{2+} , decreasing the number of $[\text{Zn}(\text{H}_2\text{O})_6]^{2+}$ species. However, the high salt concentration increases cost, undermining the affordability of aqueous electrolytes. Moreover, the high viscosity of highly

concentrated electrolytes reduces the ionic conductivity compared to dilute electrolytes [96].

Formation of solid electrolyte interphase (SEI) is another electrolyte design strategy. The SEI is formed as a byproduct of electrolyte decomposition. It enables ion transport while preventing direct contact between Zn metal and liquid electrolytes [96], [98]. However, the components in conventional aqueous electrolytes cannot form a good SEI [43]. In aqueous systems, functional SEI layers can instead be created in situ through the reduction of organic additives that are added to an aqueous electrolyte. Suitable additives are selected based on their molecular orbital energies, specifically those with higher HOMO (Highest Occupied Molecular Orbital) and lower LUMO (Lowest Unoccupied Molecular Orbital) levels than water. This ensures that the additives are reduced prior to hydrogen evolution, enabling the controlled formation of a protective SEI layer [99]. For instance, introducing dimethyl sulfoxide into aqueous ZnCl_2 electrolyte alters the primary solvation shell of Zn^{2+} and promotes the formation of a dense solid electrolyte interphase (SEI) composed of $\text{Zn}_{12}(\text{SO}_4)_3\text{Cl}_3(\text{OH})_{15}\cdot 5\text{H}_2\text{O} - \text{ZnSO}_3 - \text{ZnS}$. This SEI permits Zn^{2+} transport but prevents H_2O to reach the electrode surface, thereby suppressing hydrogen evolution and inhibiting Zn dendrite growth [100].

Although there are many advantages with aqueous electrolytes, they have a relatively narrow electrochemical stability window (ESW) of 1.23 V vs. SHE [77], [101], [102], which limits the application of high-voltage cathode materials and reduces the energy density of Zn-metal batteries [96]. The solvent in the electrolyte determines, to a large extent, the electrochemical stability window [103]. Unlike aqueous electrolytes, nonaqueous electrolytes can operate across a wider voltage range. For example, acetonitrile – $\text{Zn}(\text{TFSI})_2$, acetonitrile – $\text{Zn}(\text{CF}_3\text{SO}_3)_2$, and propylene carbonate – $\text{Zn}(\text{TFSI})_2$ electrolytes not only support highly reversible Zn deposition ($\geq 99\%$ Coulombic efficiency) but also provide high anodic stability up to ~ 3.8 V vs. Zn/Zn^{2+} [104].

In addition to conventional organic solvents, room-temperature ionic liquids have also been explored as electrolytes for Zn-metal batteries. For instance, an electrolyte formed by combining methylimidazole (EMI) with $\text{Zn}(\text{TFSI})_2$ ($\text{Zn}(\text{EMI})_{4.99}(\text{TFSI})_{1.01}$), showed excellent stability with a voltage window of 2.43 V vs. Zn/Zn^{2+} . During the first cycle, the TFSI anion in the solvation shell is preferentially reduced, forming a robust double-layer SEI rich in ZnF_2 , ZnS , and ZnN_x . This SEI effectively suppresses dendrite formation and facilitates reversible Zn deposition/stripping [105].

Another promising class of nonaqueous electrolytes is deep eutectic electrolytes (DEEs). These are synthesized by combining two or more hydrogen

bond donors and hydrogen bond acceptors in a specific molar ratio [106]. A key advantage of DEEs is their significantly lower melting point compared to their individual components. For example, an acetamide–Zn(TFSI)₂ eutectic electrolyte shows an anodic stability of 2.4 V vs. Zn/Zn²⁺ [107]. In this electrolyte, direct coordination between cations and anions forms large cationic complexes. This induces decomposition of TFSI before Zn deposition during initial cycling, producing a SEI layer rich in mechanically robust ZnF₂ and Zn²⁺-permeable organic components [107].

Chapter 3

Experimental and Theory

This chapter describes the experimental procedures for sample preparation, electrochemical measurements, and selected theoretical concepts used for characterization in Papers 1-3.

3.1 Preparation of electrolytes, electrode, and cellulose separator

3.1.1 Standard electrolyte (2 M ZnSO₄)

ZnSO₄·7H₂O (ACS Reagent 99%, Sigma Aldrich) was weighed and dissolved in miliQ water to form a 2 M ZnSO₄ electrolyte. This electrolyte was used in Papers 1-3.

3.1.2 Low-transition-temperature electrolyte

In Paper 3, the low-transition-temperature electrolyte was prepared by mixing anhydrous ethylene glycol (EG, 99.8%, Merck Germany) and Zn(TFSI)₂ (99.5%, Solvionic) at various molar ratios. For example, the low-transition-temperature electrolyte (1:7) was prepared by dissolving Zn(TFSI)₂ at 2.30 molality by heating the mixture to 80 °C and stirring for 2 hours to achieve a 0.125 mole fraction of Zn(TFSI)₂ in EG.

3.1.3 KVO electrode

Details of the synthesis of the K⁺ intercalated V₂O₅, abbreviated as KVO, can be found in the literature [108]. In Papers 2 and 3, KVO electrodes were prepared by grinding the active material with poly(vinylidene fluoride) and Ketjen black (70:10:20 wt%), and pressing the mixture at 3 x 10⁻³ kt to form 13 mm in diameter of self-standing electrodes, weighing between 20–30 mg.

3.1.4 Cellulose separators

Figure 3.1 illustrates the preparation of the cellulose separators, Paper 2, by solution casting. A solution of 1 wt.% cellulose nanocrystals (CNC) dispersed in water with different weights of 2,2,6,6-Tetramethylpiperidine-1-oxyl (TEMPO)-oxidized cellulose nanofibrils (TCNF) was poured into a petri dish and allowed the solvent to evaporate at room temperature for a few days.

The obtained hybrid CNC and TCNF separators, named HCT x:y, with x:y representing the weight ratio between CNC and TCNF, see Table 3.1.

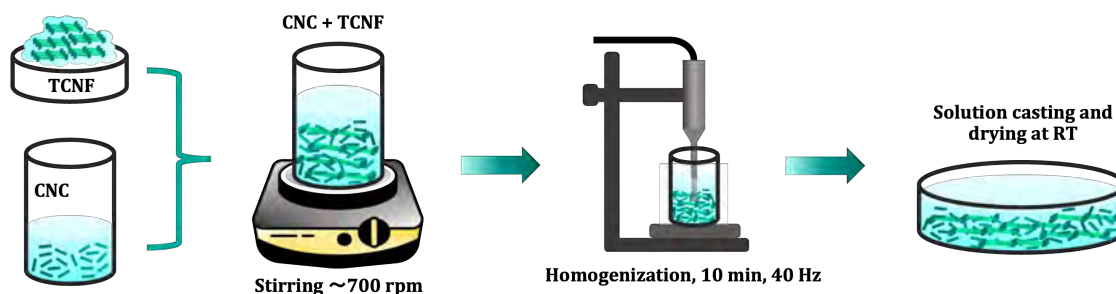


Figure 3.1: Schematic of hybrid CNC and TCNF separator (HCT) preparation via solution casting.

Table 3.1: Separator sample names and corresponding CNC:TCNF weight ratios.

Separators	Weight ratio of CNC:TCNF
CNC	-
TCNF	-
HCT 5:1	5:1
HCT 5:2	5:2
HCT 5:3	5:3

3.2 Electrolyte uptake

The electrolyte uptake of cellulose separators in Paper 2 was measured by comparing the weight of dry separators before (W_o) and after 2 h immersion in 2 M $ZnSO_4$ electrolyte (W_1). The values were calculated using Eq. (3.1).

$$\% \text{ Electrolyte uptake} = \frac{W_1 - W_o}{W_o} \times 100\% \quad (3.1)$$

3.3 Electrochemical experiments

3.3.1 Electrochemical cells

In Papers 2 and 3, coin cells (CR2032, Wellcos) were used for electrochemical measurements. The coin cells consist of top and bottom caps, a gasket, spring, and spacer, as shown in Figure 3.2a. The coin cells were used to measure cycling stability of symmetric Zn cells and Zn||KVO cells, and asymmetric Zn||Cu and Zn||Ti cells for Coulombic efficiency (CE) and linear sweep voltammetry measurements.

Besides the coin cell, Swagelok cells were used in Paper 2 to measure ionic conductivity and to deposit Zn on the Ti electrode before SEM imaging. The

Swagelok cell consists of stainless steel plungers, spring, spacer, perfluoroalkoxy (PFA) tube fitting with PFA front and back ferrules, as shown in Figure 3.2b.

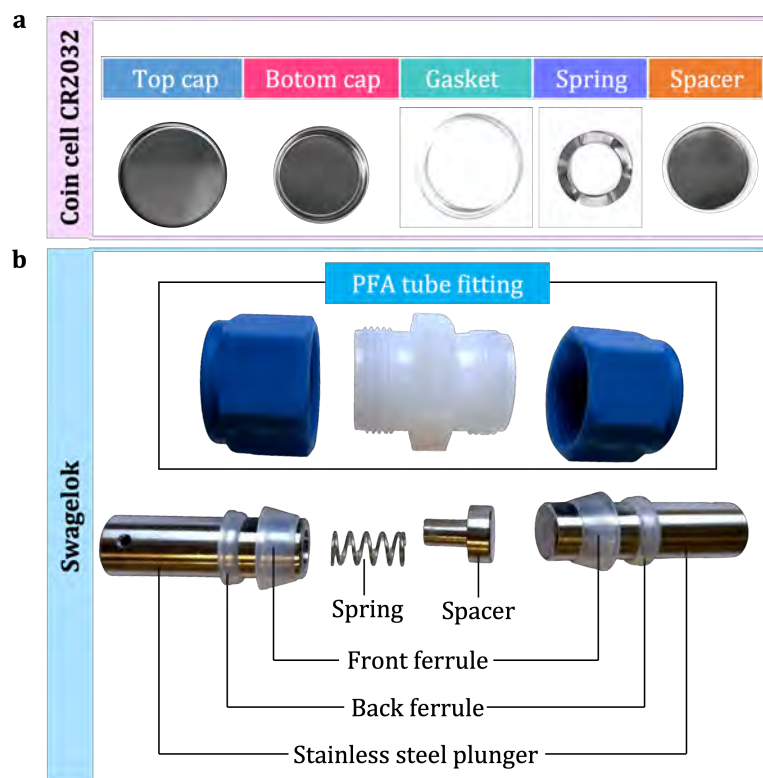


Figure 3.2: Components of (a) coin cell CR2032 and (b) Swagelok cell.

3.3.2 Electrochemical impedance spectroscopy

The ionic conductivity (σ) of separators soaked in 2 M ZnSO_4 aqueous electrolyte in Paper 2 was evaluated using electrochemical impedance spectroscopy measurement at room temperature in Swagelok Ti||Ti cells. The experiment was performed using a Biologic VMP3 with an amplitude of 5 mV and for frequencies ranging from 500 kHz to 10 Hz. The ionic conductivity was calculated using Equation (3.2), where L is the thickness of the separator after swelling with electrolyte, S is the contact area of the electrode, and R is the intersection of the semicircle in the Nyquist plot with the real impedance axis (Figure 3.3). The fitting was done on Biologic EC-Lab software.

$$\sigma = \frac{L}{SR} \quad (3.2)$$

3.3.3 Linear sweep voltammetry

Linear sweep voltammetry (LSV) is used to measure the anodic and cathodic stability of electrolytes, and from this, the electrochemical stability window

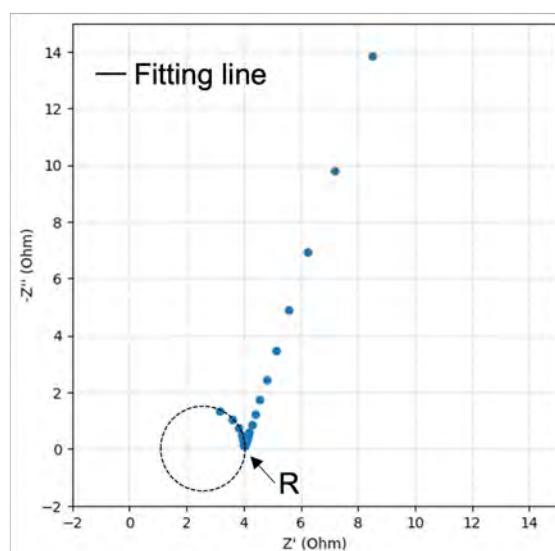


Figure 3.3: Representative Nyquist plot, showing the fitting line where the intercept indicates the electrolyte resistance (R).

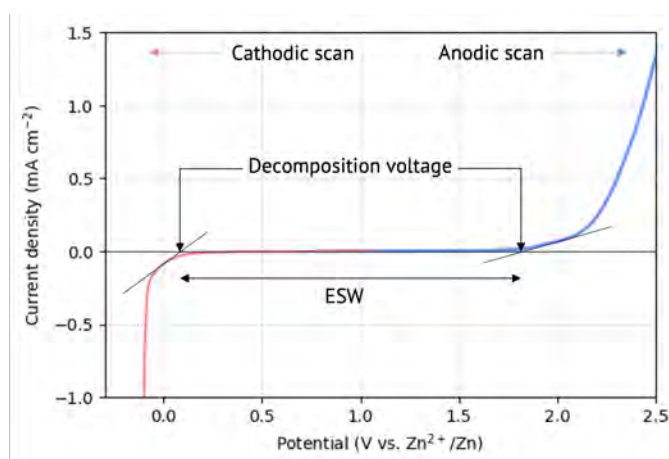


Figure 3.4: Example of LSV curve of aqueous 2 M ZnSO₄, depicting the voltages at which the electrolyte starts to degrade.

(ESW) is determined. The anodic and cathodic stabilities refer to the highest and lowest voltages at which a battery can operate without electrolyte decomposition [109]. The typical cell configuration is a two-electrode setup, in which the potential is swept linearly while measuring the resulting current at the working electrode [110], [111]. Figure 3.4 shows a typical LSV curve where the asymmetric cell was scanned from open circuit voltage (OCV) up to 2.5 V. An increase in current is taken as an indication of degradation of the electrolyte at the working electrode interface. The onset can be more accurately determined from the x-intercept of the tangent of the first step of the current increase [109].

The electrochemical stability window of the low-transition-temperature electrolyte in Paper 3 was measured using LSV. A CR2032 coin cell was

assembled in ambient environment with 60 μL of electrolyte 1:7 $\text{Zn}(\text{TFSI})_2\text{:EG}$ ratio and a glass fiber separator (Whatman GF/C). The coin cell had a Zn foil (0.1 mm, Goodfellow) as the counter electrode and composite carbon as the working electrode. The preparation for the working electrode is explained in detail in Paper 3.

3.3.4 Galvanostatic cycling

To study Zn deposition and stripping (Papers 1-3), galvanostatic cycling was used with three different cell setups: (1) symmetric $\text{Zn}||\text{Zn}$, (2) asymmetric $\text{Zn}||\text{Cu}$ or $\text{Zn}||\text{Ti}$, and (3) $\text{Zn}||\text{KVO}$.

Symmetric $\text{Zn}||\text{Zn}$

To measure the Zn deposition/stripping overpotentials of an electrolyte, a symmetric cell with the electrolyte or electrolyte-soaked separator, sandwiched between two Zn foils, was used. The symmetric Zn cell was cycled at a fixed current and fixed capacity over a number of cycles, and the resulting potential, reflecting the overpotential, was recorded. As shown in Figure 3.5, each discharge step is followed by a current reversal for the same duration, and this cycle is repeated to assess the long-term stability of the Zn anode in the given electrolyte. Lower overpotentials typically indicate lower interfacial resistance, and higher ionic conductivity of the electrolyte.

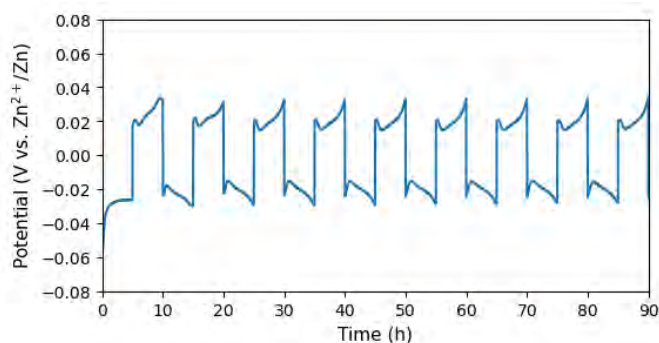


Figure 3.5: Example of galvanostatic discharge/charge of symmetric $\text{Zn}||\text{Zn}$ at 1 mA cm^{-2} and 5 mAh cm^{-2} with 2 M ZnSO_4 electrolyte.

Unless otherwise stated in both Papers 2 and 3, symmetric Zn cells were assembled with Whatman glass fiber (GF/C) or the HCT as separators, and with the 2 M ZnSO_4 electrolyte (Paper 2) or low-transition-temperature electrolyte (Paper 3).

Asymmetric Zn || Ti or Zn || Cu

Galvanostatic cycling can also be used to investigate the reversibility of Zn deposition/stripping in asymmetric Zn || Ti (Paper 2) or Zn || Cu (Paper 3) cells. The reversibility was assessed through the Coulombic efficiency (CE). In Paper 2, the CE was determined by applying a constant current to the cell until the desired amount of deposited Zn was achieved on a Ti electrode, followed by Zn stripping from the Ti electrode until a cut-off voltage of 0.4 V was reached. The CE was calculated by the amount of charge passed during deposition (Q_p) divided by the amount of charge passed during stripping (Q_s):

$$\text{CE: } \frac{Q_p}{Q_s} \quad (3.3)$$

In Paper 3, an alternative method was used to determine the CE [112], [113], as shown in Figure 3.6. The difference with the previous method is that initially, a certain amount of Zn was deposited and stripped on a Cu current collector, followed by another deposition of Zn at a fixed areal capacity, referred to as Zn reservoir (Q_r). Then, the cell was cycled for m times at a fixed, but lower capacity of Zn (Q_c) before all Zn was stripped from the Cu current collector (Q_s). The average CE was then determined using the following equation [112], [113]:

$$\text{CE: } \frac{mQ_c + Q_s}{mQ_c + Q_r} \quad (3.4)$$

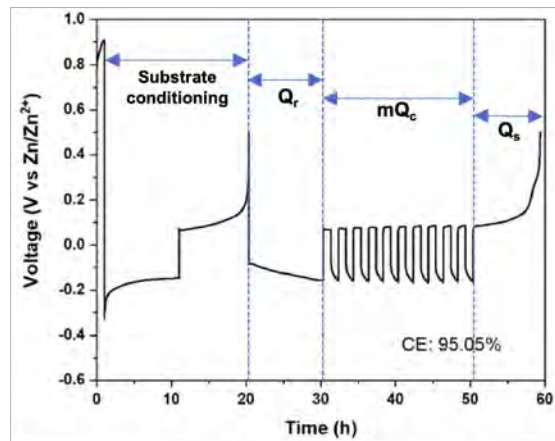


Figure 3.6: Example of voltage vs. time profiles of galvanostatic cycling protocol for evaluating Coulombic efficiency in Paper 3. Reproduced under Creative Commons license. Copyright 2025 Elsevier.

Asymmetric Zn || KVO full cells

To evaluate the performance of full cells, galvanostatic cycling was performed with Zn || KVO cells. Here a current was applied at a given rate (A g^{-1}) with respect to the active material weight of the KVO electrode, and the voltage response was measured with voltage limits being applied (V_1) and (V_2), as shown in Figure 3.7. These measurements provide information on capacity by measuring how long the current is sustained before reaching the voltage cut-off limit, rate capability by observing the effect of increased applied current on the capacity, and CE. After prolonged galvanostatic cycling, comparisons can be made between cycles to determine capacity decay or changes in cell polarisation.

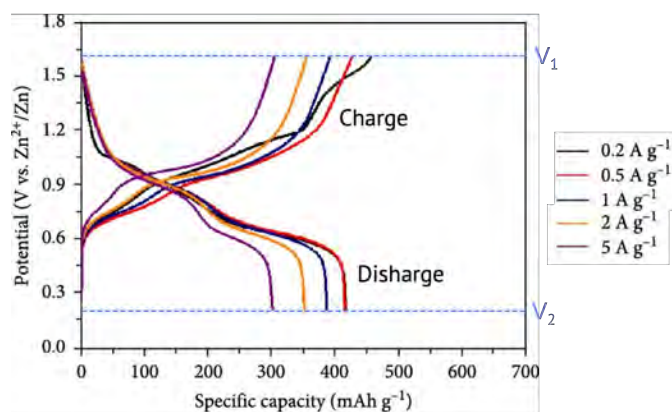


Figure 3.7: Example of a galvanostatic voltage profiles of Zn|| V_2O_5 at different current densities ranging from 0.2 to 5 A g^{-1} . Reproduced from Yoon et al. [71] (Copyright 2025, John Wiley & Sons), under Creative Commons Attribution License.

3.4 Imaging techniques

Imaging techniques offer the benefit of presenting information intuitively, often described as “what you see is what you get” [114]. Early battery research relied on “ex situ” imaging methods, which involve disassembling batteries at certain stages to analyze their components outside of operation. To gain deeper insights, imaging techniques need to be performed within the battery’s closed system. “*In situ*” imaging means “in place” and refers to methods that visualize battery components without disassembly, including observations at specific states before reactivation. The term “*operando*” imaging (meaning “during operation”) refers to imaging the battery while it is actively functioning, capturing the effect of electrochemical reactions in real time. Both *in situ* and *operando* techniques are essential for accurately monitoring processes inside working batteries [115].

Paper 1 primarily uses *operando* synchrotron X-ray tomography to track

Zn deposition and stripping in real time, while Papers 2 and 3 employed ex situ scanning electron microscopy (SEM) imaging of electrodes before and after cycling, and to image the surface of cellulose separators. This section provides a detailed overview of these techniques.

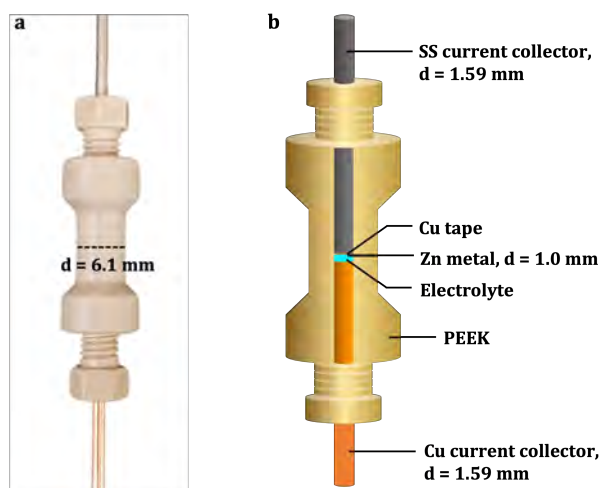


Figure 3.8: (a) Photographic image of *operando* cell and (b) schematic drawing of *operando* cell and its components.

3.4.1 *Operando* synchrotron X-ray tomographic microscopy

Operando cell setup

For synchrotron X-ray tomographic microscopy (XTM) experiments, a special cell was designed, adapted from Sadd et al. [116]. Figures 3.8a,b show a photograph of the *operando* cell (a) and a sketch of the cell components (b). There are several considerations to take into account for the design of the cell: (1) the size of the cell and the geometry, (2) X-ray transparency, and (3) sample mounting. The inner diameter of the cell allows a maximum electrode size of 1.59 mm. This size was chosen to match the field of view when using a 10x objective at the TOMCAT beamline at PSI. The housing of the cell was made of polyether ether ketone (PEEK), which has relatively low X-ray absorption, thereby minimizing interference with the X-ray beam and reducing background noise. PEEK is also resistant to many chemicals, which prevents contamination of the samples. Furthermore, the geometry and size of the cell need to be compatible with the beamline, securely mounted on the sample stage, and allow for electrical connections.

Synchrotron X-ray tomography experiment

Figure 3.9 shows the setup for the experiment, with the *operando* cell placed between the X-ray source and the detector, and connected to a potentiostat

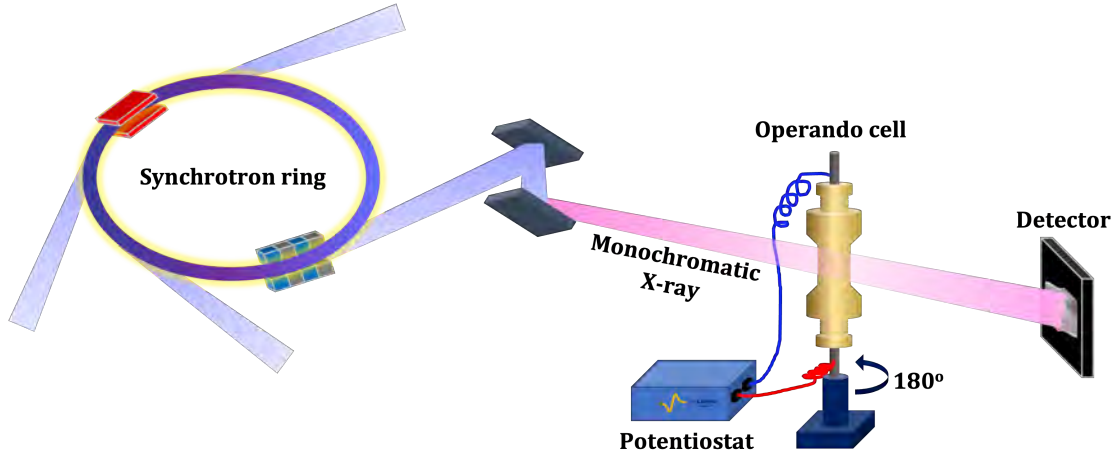


Figure 3.9: Illustrations of *operando* experiment XTM setup. Inspired from Ref. [117].

(Biologic SP300). A synchrotron X-ray beam with an energy of 20 keV was chosen to maximize the contrast of the cell components. Images were taken before, during, and after galvanostatic cycling, with a half-acquisition method (rotating the sample up to 180°). For every scan, a total of 1,000 projections were recorded with a typical exposure time per projection of 50 ms.

As the X-rays pass through the cell, they are partially absorbed by the materials. The transmitted X-rays are detected by a scintillator and detector to produce 2D cross-sectional images. These images reflect how much the X-rays were attenuated, a process explained by the Beer–Lambert law [118]:

$$I = I_0 e^{-\mu d} \quad (3.5)$$

where I and I_0 represent the intensity of the transmitted and incident X-rays, respectively, d is the attenuation length, and μ is the linear absorption/attenuation coefficient. The attenuation coefficient is unique to each material and allows the differentiation of components within the cells. Due to differences in linear attenuation coefficient (μ) [119], [120]:

$$\mu = \frac{4\pi\beta}{\lambda} \quad (3.6)$$

where λ is the X-ray wavelength and β is the material specific attenuation coefficient (absorption). In absorption contrast tomography, the main interaction between X-rays and the sample is absorption, and β is defined as:

$$\beta = \frac{h^4 c^4}{2\pi} \rho \frac{Z^3}{E^4} \left[\frac{1}{\text{m}} \right] \quad (3.7)$$

where ρ , Z , E , h , and c are the electron density of the material, atomic number of

the material, beam energy, Planck constant, and the speed of light, respectively. The resulting image contrast is the differences between different $\beta(\Delta\beta)$ [119]. We can infer from this equation that a large difference in Z gives high contrast. It also means that, although Z is large, if two materials have similar Z values, they might still be difficult to separate.

Image analysis

The general workflow of image analysis is illustrated in Figure 3.10. The reconstructed image was first filtered with a median filter to decrease noise in the image. The median filter was selected since it preserves the edges of objects. The next step is to choose the volume of interest by cropping. After that, image segmentation is used to separate the component of interest from other components. In Paper 1, the goal was to separate the Zn deposits from the other cell components. Here, a thresholding-based segmentation was applied. The segmented image is a binary image, consisting of black and white images with values of either 0 or 1. Typically, 0 is assigned for foreground and 1 is assigned to the segmented object. From this binary image, 3D volume rendering or quantitative image analysis can be done. The volume rendering was performed using Paraview software, while the other image analysis was conducted with home-built Python scripts.

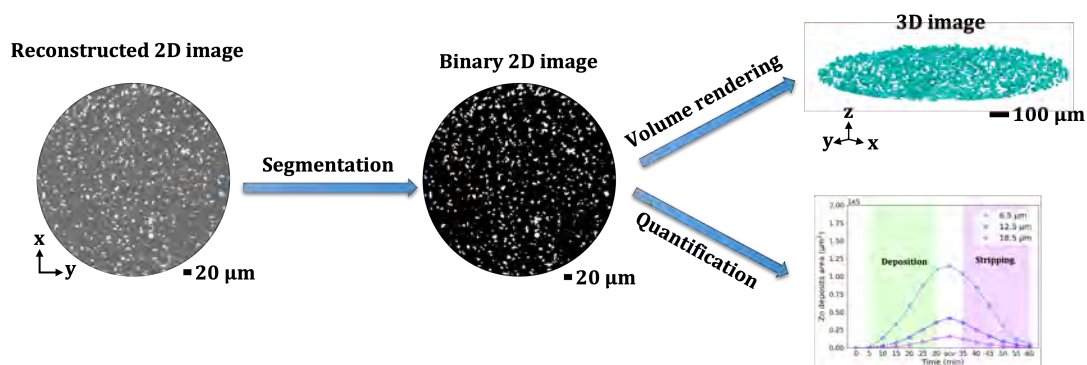


Figure 3.10: Workflow for image processing and analysis.

3.4.2 Scanning electron microscopy

In Paper 2, SEM (JEOL JSM-7800F Prime) was used to characterize the electrodes and cellulose separators after cycling. This method was also employed in Paper 3 (SEM Phenom ProX, Thermo Fisher) to image the Zn anode before and after cycling with low-transition-temperature electrolyte (1:7) and 2 M ZnSO_4 electrolyte.

In SEM, high-energy electrons (typically 2–40 keV) from an electron gun interact with the sample, generating signals that are detected to form detailed

images [121], [122]. When the primary electron beam interacts with the sample surface, it produces various signals that are collected by different types of detectors in the SEM chamber, such as secondary electrons, backscattered electrons, Auger electrons, characteristic X-rays, and cathodoluminescence [121], [122], [123], as illustrated in Figure 3.11. Secondary electrons provide surface topography, while characteristic X-rays are analyzed and quantified by energy dispersive X-ray spectroscopy (EDS) to determine elemental composition [122], [123], [124].

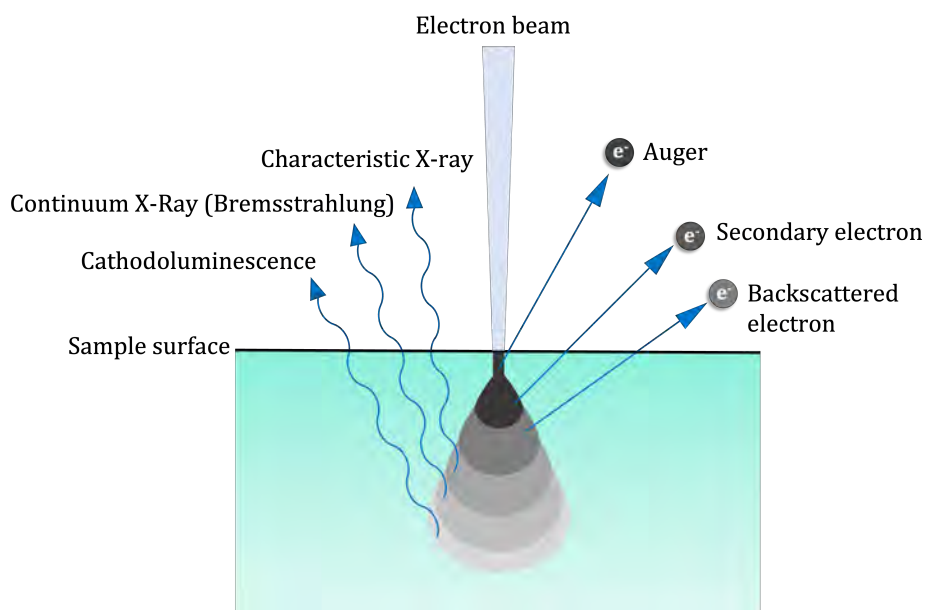


Figure 3.11: Illustration of various signals produced by electron beam and sample interaction in SEM and the regions from which the signals can be detected. Adapted in part with permission from Liu et al. [123]. Copyright 2025 American Chemical Society.

SEM sample preparation

The samples were mounted on SEM stubs with electrically conducting pads (PELCO Tab), Carbon Conductive Tabs, 12 mm OD). To effectively use SEM, samples often need to be conductive. Non-conductive specimens, like biological materials, are typically coated with a thin layer of gold to prevent charge buildup, which can distort images [124], [125]. The charging effect occurs when electrons accumulate in certain areas, leading to image distortion [124]. The coating helps dissipate excess electrons by homogenizing surface charge and is the standard method in high-vacuum conditions [124]. In Paper 2, since the cellulose separators are nonconductive, an ultra-thin conductive Au layer was applied (~ 2 nm) using Leica EM sputter coater. For Zn electrodes, the images were obtained without any coating. However, before SEM imaging, the Zn electrodes were taken from coin cells and washed. In Paper 3, the Zn electrodes

retrieved from the Zn||KVO cells were washed with water and dried, then subsequently treated in an ultrasonic bath at 60 kHz for 15 minutes in water, followed by a second drying step.

3.5 Vibrational spectroscopy

Vibrational spectroscopy techniques, such as Raman and Fourier transform infrared (FTIR) are highly valuable tools for probing molecular structures and interactions. The two techniques differ in their interaction with molecular vibrations, making them highly complementary, and using them together offers a powerful tool for structural characterization [126].

Raman spectroscopy involves inelastic photon scattering due to a change in polarizability of a molecule, that is, how readily its electron cloud can be distorted by the incident monochromatic light [126], [127]. When monochromatic light interacts with molecules, it can be scattered elastically or inelastically, as shown in Figure 3.12a. Elastic scattering (Rayleigh) occurs when scattered light has the same frequency as the incident beam. In inelastic scattering, the scattered light has a different frequency than the incoming light. When a photon loses energy to the molecule's vibrations, the scattered photon has a lower frequency than the original light, and this is called Stokes Raman scattering. If the photon gains energy from the molecule's vibrations (phonons), the scattered photon will have a higher frequency than the incoming light, and this is called anti-Stokes Raman scattering [126], [128].

FTIR spectroscopy detects molecular vibrations that result in a change in dipole moment by measuring the absorption of molecule-specific wavelengths from polychromatic light [126], [127]. Among the various IR spectroscopy techniques, attenuated total reflection (ATR)-FTIR spectroscopy is one of the most widely used [129]. This method is suitable for analyzing liquid or solid samples placed directly on an ATR crystal (e.g., ZnSe, diamond, germanium, and silicon), thereby eliminating the need for complex sample preparation [127]. In ATR-FTIR, the light undergoes internal reflection at the interface between the crystal and the sample, as illustrated in Figure 3.12b. When the refractive index of the crystal is higher than that of the sample, the incident IR beam undergoes total internal reflection at the interface, generating an evanescent wave that penetrates the sample to a certain depth. Depending on the crystal shape, the IR beam may reflect once for higher spatial resolution or multiple times to increase signal strength [127]. The reflected beam travels to the detector, where an interferogram is generated and processed into a spectrum [129].

In Paper 2, FTIR spectroscopy was used for identification of functional

groups in cellulose separators in comparison with CNC and TCNF separators. In Paper 3, both FTIR and Raman spectroscopies were used to probe the local structures of the low-transition-temperature electrolyte.

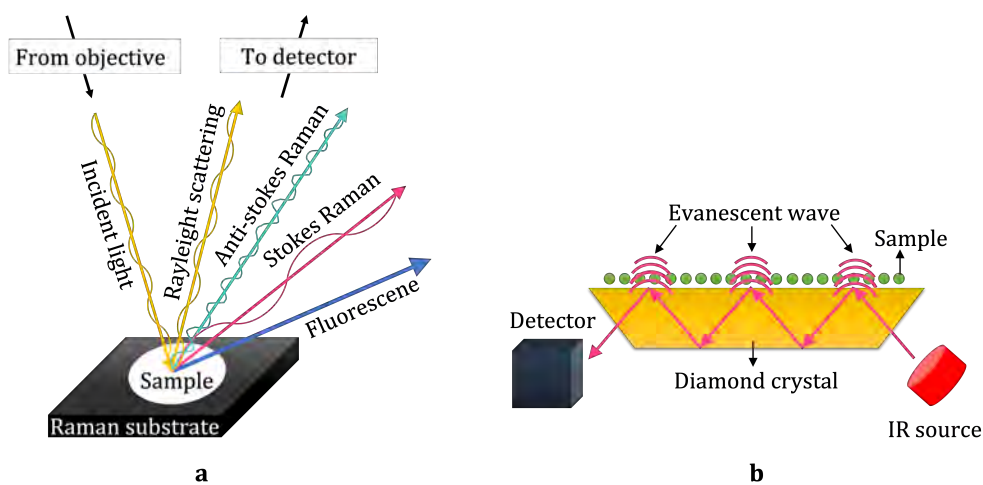


Figure 3.12: (a) Schematic drawing of light scattering when the sample is exposed to a monochromatic beam. Adapted in part with permission from Agrawal et al. [128]. Copyright 2018 American Chemical Society. (b) ATR-FTIR experiment. Adapted with permission from Weber et al. [129]. Copyright 2023 American Chemical Society.

Chapter 4

Results and Discussion

This chapter presents the findings from Papers 1-3. The discussion is organized based on three research questions: (i) how Zn microstructures evolve during deposition and stripping, and how this relate to the reversibility of the Zn anode (Paper 1), (ii) how separator design affects Zn deposition morphology (Paper 2), and (iii) how electrolyte composition influences Zn^{2+} solvation and interfacial stability of the Zn anode (Paper 3).

4.1 Mechanisms of Zn deposition and stripping

The electrochemical reversibility of the Zn metal anode is strongly influenced by the evolution of the morphology during Zn deposition and stripping [130]. However, the relationship between the morphology and electrochemical reversibility remains unclear. To address this, we employed *operando* synchrotron X-ray tomography to directly visualize Zn growth and dissolution in 3D at a Cu current collector during the first cycle. While the configuration with an asymmetric Zn||Cu cell without a separator does not fully represent a practical Zn-metal battery, it enables high-resolution observation of deposition and stripping processes, providing crucial mechanistic insights into how morphology affects the reversibility of the Zn anode.

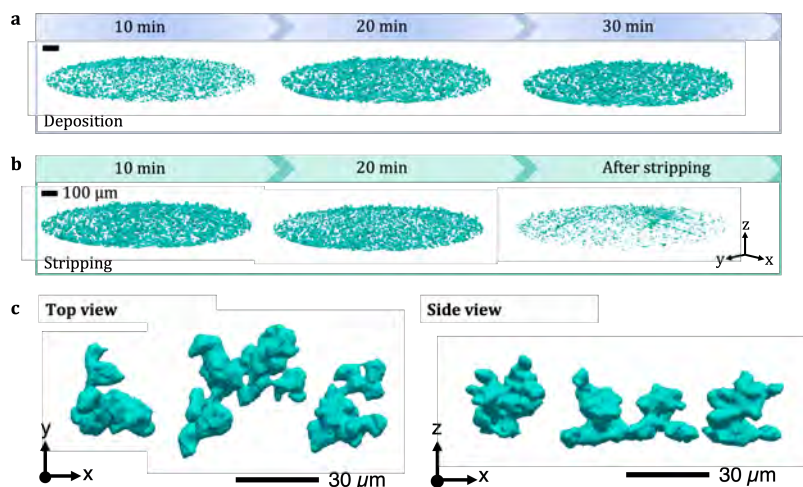


Figure 4.1: 3D renderings of segmented Zn deposits at selected (a) deposition and (b) stripping time at a current density of 10 mA cm^{-2} and an areal capacity of 5 mAh cm^{-2} , and (c) individual Zn deposits at the end of deposition.

Figures 4.1a,b depict 3D volume renderings of segmented Zn during Zn deposition and stripping on the Cu current collector at a current density of 10 mA cm^{-2} . During deposition (Figure 4.1a), Zn deposits grow both vertically and laterally across the Cu substrate. Figure 4.1c shows that at end of deposition, 5 mAh cm^{-2} , Zn deposits with different thicknesses and sizes are found. Conversely, the amount of Zn gradually decreases with time during stripping, reflecting the dissolution of Zn metal (Figure 4.1b). However, even after reaching the stripping cut-off potential ($0.4 \text{ V vs. Zn/Zn}^{2+}$), there is still Zn left on Cu current collector, indicating incomplete dissolution of the Zn. This is evidenced by the Coulombic efficiency obtained from electrochemistry data (Figure 4.2a) and imaging data (Figure 4.2b), that are 94.5% and 93.7%, respectively.

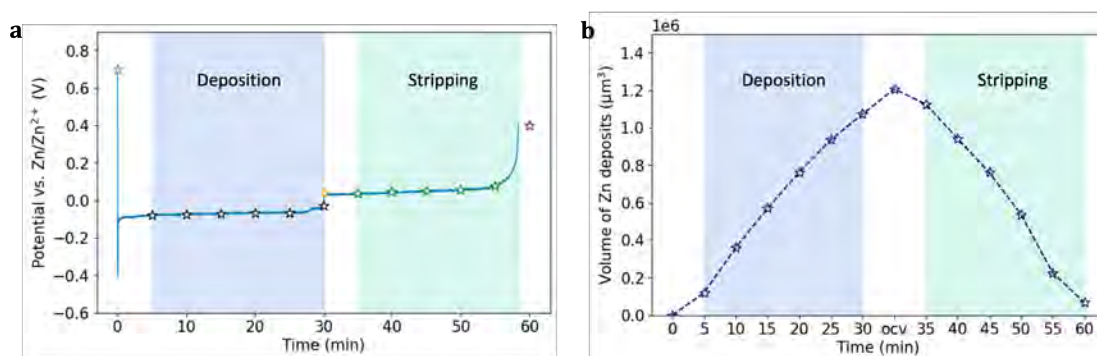


Figure 4.2: (a) Voltage versus time profile during XTM experiment and (b) changing in the volume of Zn deposits from image analysis. The stars indicate where the tomograms were taken.

To further understand the evolution of the morphology, we isolated a smaller 3D volume rendering of Zn. Figure 4.3a shows the volume of interest during Zn deposition. The *operando* 3D images reveal two different growth modes during deposition: (i) successive deposition on existing Zn deposits, resulting in thickening, and (ii) coalescence of smaller Zn deposit into larger deposits. During stripping (Figure 4.3b), dissolution occurs at the tip and root of Zn deposits at different rates. This causes the fragmentation of larger clusters into smaller ones during stripping. When the stripping occurs from the root, it causes detachment of Zn deposits from the Cu electrode, leaving Zn that is electronically disconnected from the Cu electrode, known as dead Zn [131], [132]. The accumulation of dead Zn on the electrode can cause passivation of the electrode surface and reduce the amount of electrochemically active material, leading to irreversible capacity loss [133], [134]. This finding suggests that strategies to regulate morphology are critical for improving Zn anode reversibility.

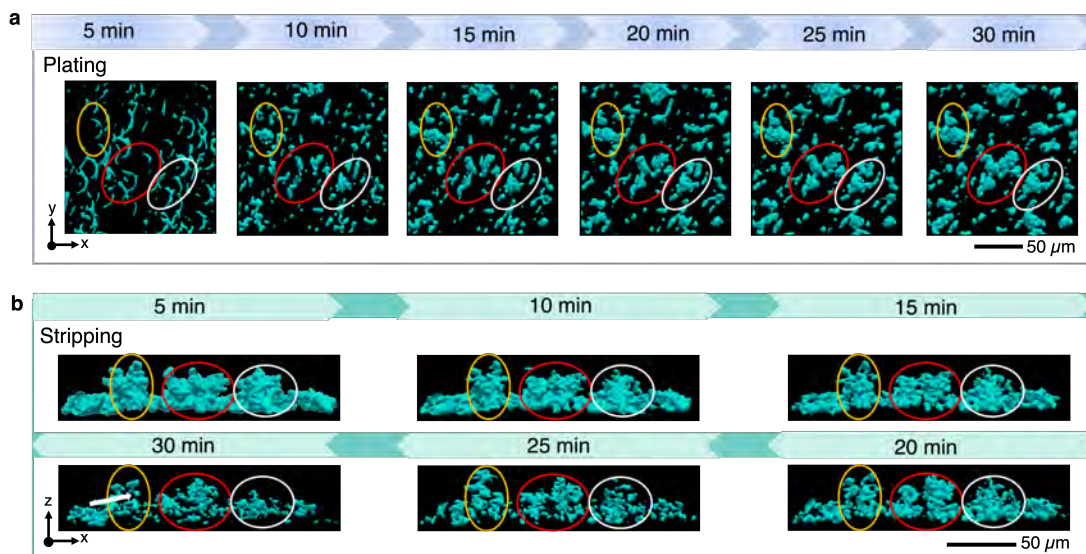


Figure 4.3: (a) Top view of 3D Zn deposits at various deposition times. (b) Side view of 3D images of Zn deposits at different stripping times. Yellow, red, and white ovals indicate the formation of large Zn clusters at three locations. The white arrow shows the fragmentation and detachment of a Zn deposit from the Cu surface.

4.2 Separator design

A separator must both keep the anode and cathode apart and retain enough electrolyte to enable efficient ions transport [135]. Beyond these basic roles, separators can also be functionalized to regulate interfacial chemistry and further enhance battery performance [136]. In Paper 3, we developed a hybrid functional separator made of cellulose nanocrystal (CNC) and TEMPO-oxidized cellulose nanofibrils (TCNF), named HCT, to tailor Zn deposition.

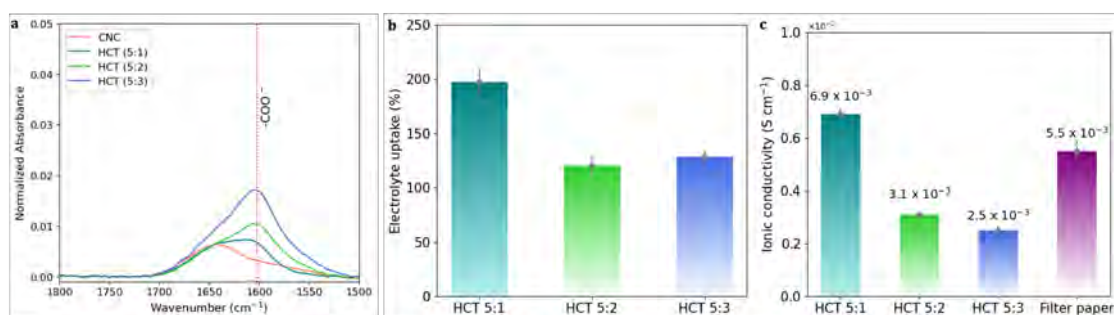


Figure 4.4: (a) FTIR spectra of CNC and HCT separators in the range between 1800-1500 cm^{-1} . The red dashed-line highlights the carboxyl ($-\text{COO}^-$) peak. (b) Electrolyte uptake of the HCT separators after 2 h immersion in 2 M ZnSO_4 aqueous electrolyte. (c) Ionic conductivity of HCT separators and commercial filter paper after soaking in 2 M ZnSO_4 aqueous electrolyte.

Figure 4.4a shows that the HCT separators exhibit a peak at 1602 cm^{-1} , attributed to carboxyl groups ($-\text{COO}^-$) [137] after TCNF addition, confirming successful incorporation. The presence of these hydrophilic groups improves

electrolyte uptake (Figure 4.4b) and ionic conductivity (Figure 4.4c) of the HCT separator to some extent. Among the HCT separators, HCT 5:1 achieves the highest electrolyte uptake, and its ionic conductivity even surpasses that of commercial filter paper. This suggests that HCT 5:1 provides efficient ion transport channels that enables uniform Zn deposition and suppressing the uneven growth that leads to dead Zn [138], as discussed in Section 4.1.

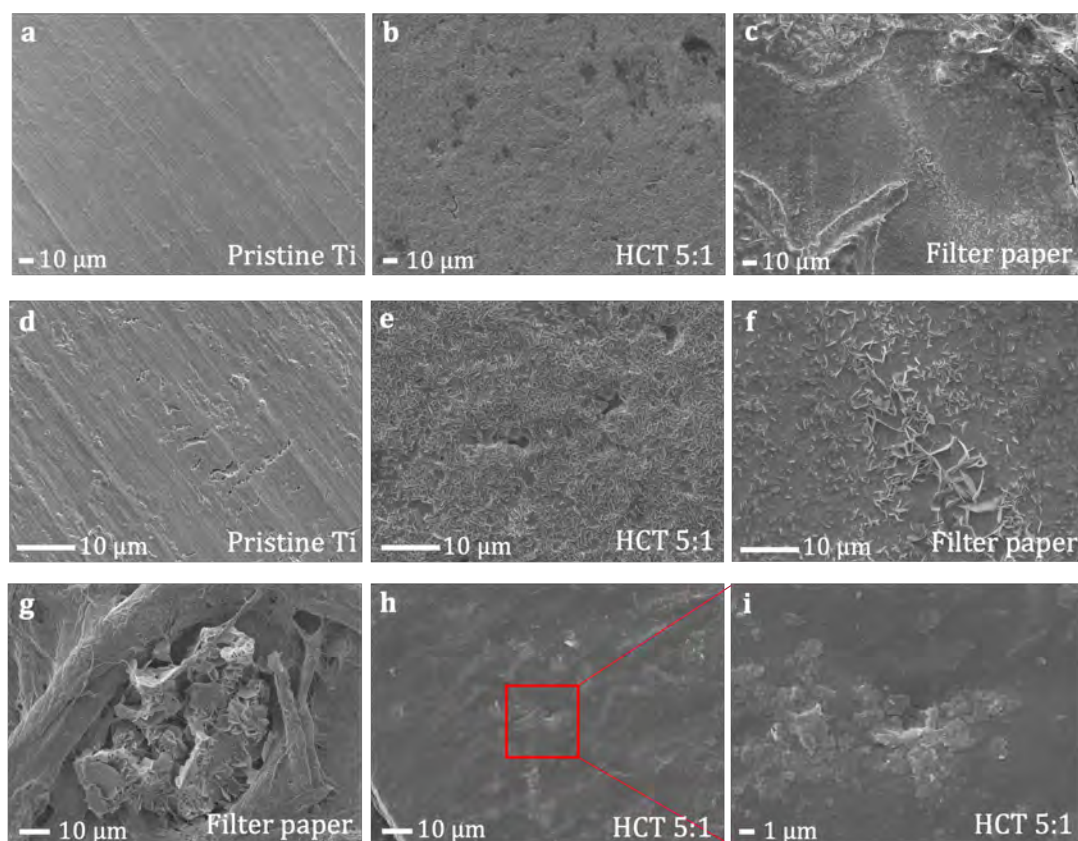


Figure 4.5: SEM images of (a) pristine Ti current collector and Zn deposited on Ti current collector using (b) HCT 5:1 and (c) filter paper separators, at 1 mA h cm^{-2} and 10 mA cm^{-2} . The images on (d-f) show higher magnifications of (a-c). Surface morphology of cycled separators after deposition under the same conditions: (g) filter paper, (h) HCT 5:1, and (i) higher magnification of (h).

To assess the influence of separator chemistry on Zn growth, the Zn deposition morphology after first deposition on a Ti current collector was examined using SEM (Figure 4.5a-f). The HCT 5:1 facilitated the formation of uniformly distributed Zn deposits (Figure 4.5b,e), whereas the commercial filter paper resulted in deposits of varying sizes and inhomogeneous distribution (Figure 4.5c,f). In particular, Zn tended to accumulate within the pores of the filter paper, forming irregularly shaped deposits (Figure 4.5g). By contrast, the HCT 5:1 effectively suppressed the formation of harmful, sharp Zn deposits (Figure 4.5h,i). The SEM results also confirm that chemical functionalization effectively regulates the initial growth of Zn. This early

morphological control is critical, as demonstrated in Section 4.1, because cluster merging and irregular shape during deposition promote fragmentation and the formation of electrochemically inactive Zn.

The influence of morphological control on practical battery performance was assessed using symmetric Zn||Zn and Zn||Ti cells (Figure 4.6a,b). Both Zn||Zn and Zn||Ti cells with HCT 5:1 separator exhibited longer cycling lifetimes than with filter paper separator. The HCT 5:1 separator enabled improved reversibility with an average Coulombic efficiency of 98.8% after 100 cycles. These results demonstrate that early growth regulation via separator functionalization leads to improved reversibility and mitigates the formation of dead Zn, as identified in Section 4.1. To demonstrate the practical application of HCT 5:1, a full cell with KVO cathode was measured. Figure 4.6c shows the voltage vs. specific capacity of Zn ||KVO with HCT 5:1 separator. In the first cycle, the cell exhibited a specific capacity of 150 mAh g⁻¹. Figure 4.6d shows that the capacity decreases over first 10 cycles but then recovers and maintains a stable discharge capacity of 150 mAh g⁻¹ up to 100th cycles.

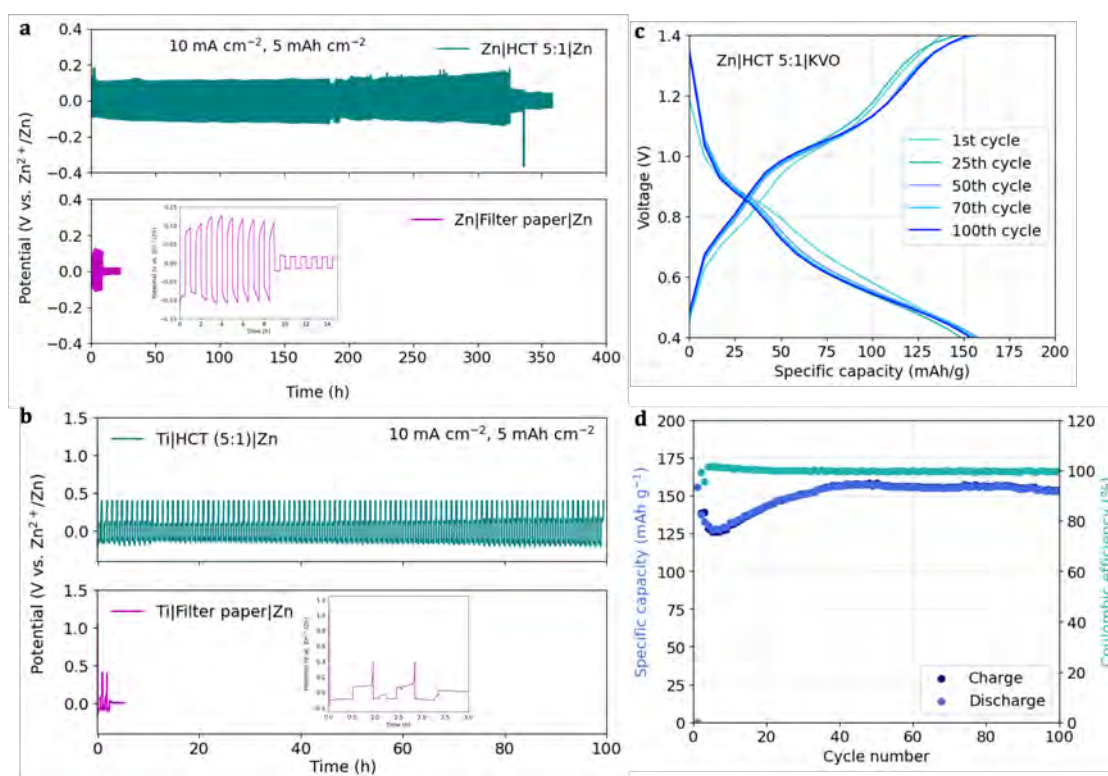


Figure 4.6: (a) Zn||Zn and (b) Zn||Ti cells with HCT 5:1 and filter paper separators cycled at 10 mA cm⁻² and 5 mAh cm⁻². (c) Selected galvanostatic discharge/charge curves and (d) long-term cycling performance of Zn||KVO with HCT 5:1 separator at a current density of 0.5 Ag⁻¹.

4.3 Electrolyte engineering

Nonaqueous electrolytes have the potential to broaden the electrochemical stability window and inhibit interfacial reactions, such as the hydrogen evolution [139]. In Paper 3, we developed a new nonaqueous electrolyte consisting of $\text{Zn}(\text{TFSI})_2$ and ethylene glycol (EG) with the aim to modify the primary solvation structure of Zn^{2+} and to improve the electrochemical stability window.

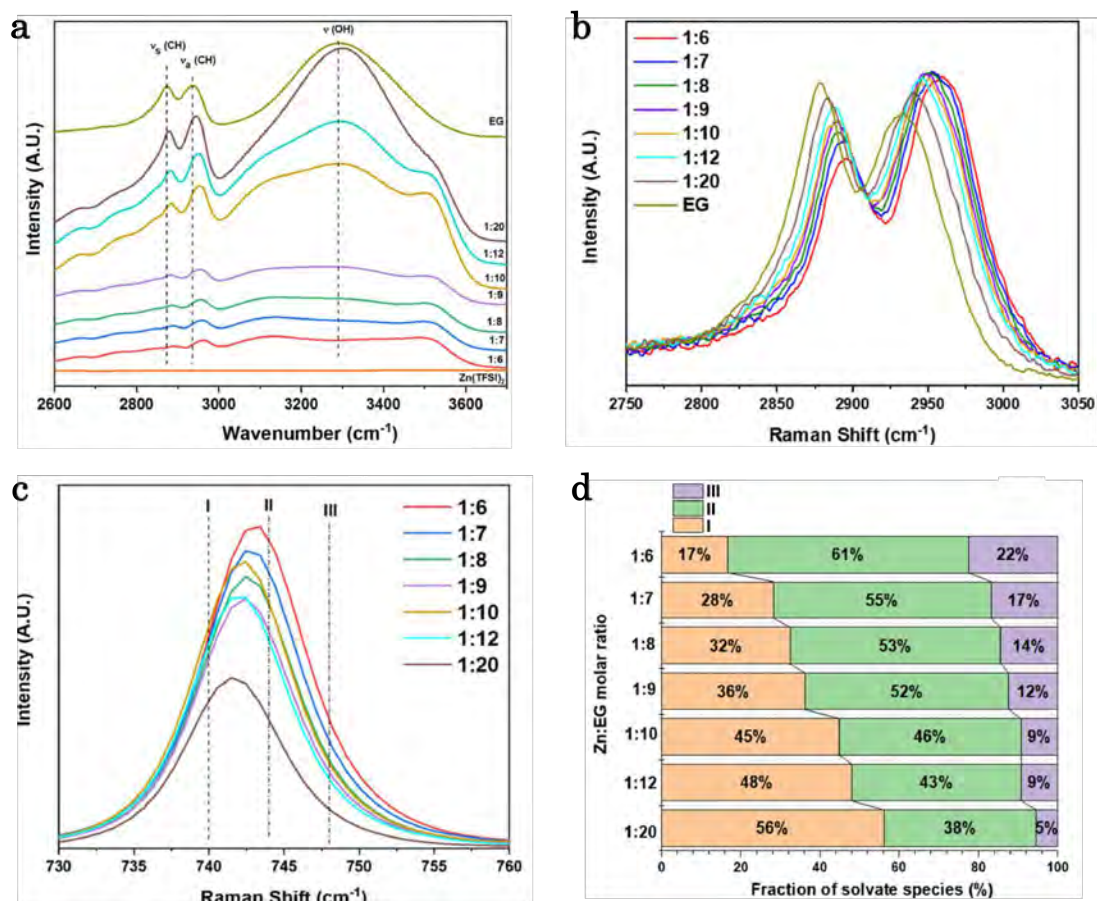


Figure 4.7: (a) ATR-FTIR spectra of ethylene glycol (EG), ZnTFSI_2 , and various low-transition-temperature electrolyte ratios. Raman spectra in the regions of (b) 2750 and 3050 cm^{-1} and (c) 730 and 760 cm^{-1} . (d) Peak areas fitted from the Raman spectra in (c). Figures are from Paper 3, reproduced under Creative Commons license. Copyright 2025 Elsevier.

To probe the local structure of our low-transition-temperature electrolytes, we employed FTIR and Raman spectroscopy. In Figure 4.7a, the FTIR spectra of low-transition-temperature electrolytes with different $\text{Zn}(\text{TFSI})_2$:EG molar ratios are shown. A decrease in the $-\text{OH}$ stretching peak at 3300 cm^{-1} upon increasing salt content indicates weakening $-\text{OH}$ bonds between ethylene glycol. The appearance of shoulder peak near 3500 cm^{-1} suggests stretching of free O-H bond in ethylene glycol that do not form H-bonds. An observed blue shift in FTIR for the C-H stretching bands at 2873 cm^{-1} and 2936 cm^{-1} , supported

with the Raman spectra in Figure 4.7b, indicate the weakening bonds between ethylene glycol after salt addition.

Further deconvolution of the Raman band between $730\text{-}760\text{ cm}^{-1}$ of the TFSI anion (Figure 4.7c) reveals three distinct regions: Region I at 740 cm^{-1} corresponding to free TFSI anion in the C1 configuration, Region II at 744 cm^{-1} corresponding to free TFSI anion in the C2 configuration, and Region III at 751 cm^{-1} corresponding to TFSI anion coordinated with Zn^{2+} . Figure 4.7d shows the Raman band deconvolution results of the fraction of the different TFSI anion configurations: free and associated to Zn^{2+} across varying low-temperature-transition electrolyte concentrations, which indicates that $\geq 12\%$ of TFSI anions are present in the solvation shell of Zn^{2+} at electrolyte molar ratios up to 1:9. This anion coordination is favorable for forming anion-derived solid electrolyte interphases (SEI) on the Zn metal anode, which can enhance interfacial stability [107], [140].

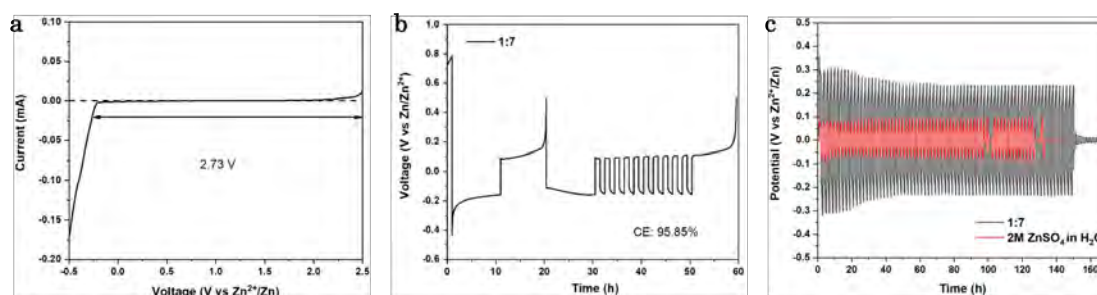


Figure 4.8: (a) LSV of LTT (1:7) at 0.2 mV s^{-1} for ESW determination. (b) Coulombic efficiency of LTT (1:7). (c) Voltage evolution vs. time for Zn||Zn symmetric cell with LTT (1:7) and standard electrolyte at 0.1 mA cm^{-2} , 0.1 mAh cm^{-2} . Figures are from Paper 3, reproduced under Creative Commons license. Copyright 2025 Elsevier.

Figure 4.8a reveals that the 1:7 low-transition-temperature electrolyte broadens the electrochemical stability window to 2.73 V. The Coulombic efficiency measured was 95.9%, as shown in Figure 4.8b. Although the value is lower than in common aqueous electrolytes, the Zn||Zn symmetric cell with low-transition-temperature electrolyte (1:7) (Figure 4.8c) extends the cycle life of the cell in comparison with 2 M ZnSO_4 at low current density of (0.1 mA cm^{-2}). These observations demonstrate that the engineered electrolyte stabilizes Zn deposition and stripping, despite the trade-off in overpotential and efficiency.

SEM images of Zn electrodes (Figure 4.9a-c), retrieved from Zn||Zn cells after 10 cycles, revealed smoother and more uniform Zn deposition with low-transition-temperature electrolyte (1:7) compared to the 2 M ZnSO_4 aqueous electrolyte. Full-cell measurement with a KVO cathode (Figure 4.9d)

confirmed the practical feasibility of the low-transition-temperature electrolyte (1:7). The full cell could be cycled up to 50 cycles with a maximum capacity of 90 mAh g^{-1} before dropping to 50 mAh g^{-1} after 50 cycles. We acknowledged that this is likely due to high viscosity of the electrolyte, which increases the cell polarization. Nevertheless, these results suggest that electrolyte design has the potential to mitigate interfacial side reactions on the Zn anode caused by the hydrogen evolution reaction, thereby promoting more uniform Zn deposition.

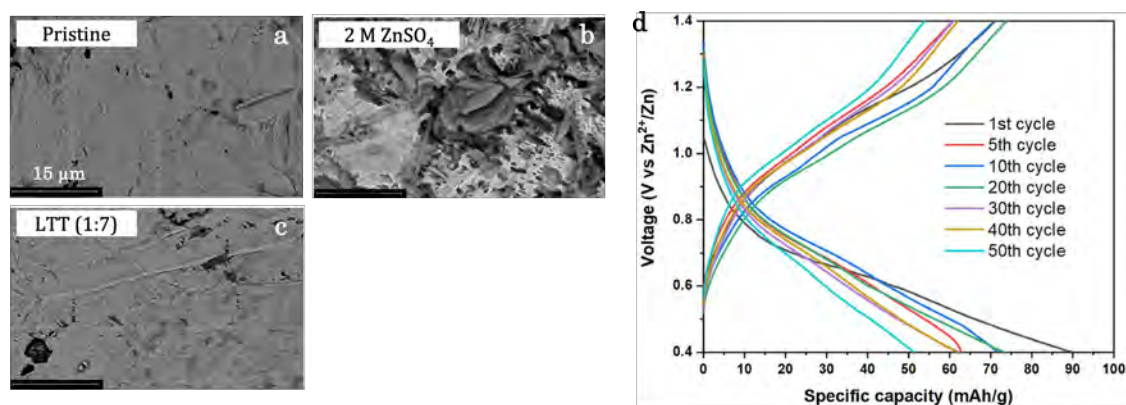


Figure 4.9: (a-c) SEM images of pristine and cycled Zn metal anode after 10 cycles in LTT (1:7) and standard electrolyte. (d) Voltage vs. specific capacity of Zn||KVO at 10 mA g^{-1} . Figures are from Paper 3, reproduced under Creative Commons license. Copyright 2025 Elsevier.

Chapter 5

Conclusions and Outlooks

Given the prospect of rechargeable Zn-metal batteries as complementary to the existing Li-ion batteries, it is crucial to pay attention to the problems on the Zn anode. This thesis has shown that strategies to stabilize the Zn anode can be built on integrating imaging techniques, separator design, and electrolyte engineering. Paper 1 uses synchrotron X-ray tomography to provide a mechanistic insight into the growth and dissolution of Zn in an aqueous electrolyte. Specifically, the initial Zn deposits guide the subsequent growth of Zn either by thickening or merging to form bigger Zn clusters during deposition, whereas stripping results in fragmentation of the Zn clusters. The finding revealed the cause of irreversibility and dead Zn formation during stripping.

Paper 2 shows a strategy to regulate Zn deposition with a hybrid CNC:TCNF separator. The hydrophilic group ($-\text{COO}^-$) enhances the electrolyte uptake and ionic conductivity of the separator, thus promoting uniformly distributed Zn deposits, improving the cycling stability, and reversibility. Paper 3 demonstrates that nonaqueous electrolytes offer the chance to extend the electrochemical stability window of the electrolyte, thus minimizing the interfacial hydrogen evolution reaction. The results showed improvement in cycle life and smoother Zn deposition. All in all, the studies presented in this thesis establish systematic design approaches for rechargeable Zn-metal batteries: early-stage deposition control and electrochemical environment optimization are both critical to improve the cycling stability of the Zn anode.

For future work, further investigation of interface engineering, such as applying liquid metal on the Zn anode or substrate, holds potential for mitigating uneven Zn deposition and interfacial side reactions on the Zn anode [71]. Pursuing multiple strategies, including separator design, electrolyte optimization, and Zn-metal anode coatings, coupled with advanced characterization techniques, represents a promising avenue for future research. This way, the potential of rechargeable Zn-metal batteries as environmentally friendly, more secure, and durable batteries can be unlocked.

Acknowledgements

An immense thank you to my PhD supervisor, Professor Aleksandar Matic, for his encouragement, patience, and guidance throughout my PhD journey so far. Thank you for introducing me to the realm of beamtime, overseas conferences, and summer schools, which not only allowed me to gain in-depth knowledge in my research area but also gave me the opportunity to explore the globe.

I sincerely thank my former co-supervisor, Professor Shizhao Xiong, for helping me prepare the beamtime at TOMCAT and for reassuring me that the experiment would work out, and it did. Discussing the results with you has always been enjoyable, as you bring a refreshing and valuable perspective.

I would like to express my gratitude to my co-supervisor, Professor Gunnar Westman, for generously sharing his expertise and providing samples for my project. I am also grateful to my examiner, Professor Patrik Johansson, for his valuable feedback on this thesis. I also thank Dr. Ezio Zhanggellini for introducing me to the laboratory and its instruments, as well as for assisting with N₂ gas refills whenever needed for measurements.

I am grateful to everyone I have collaborated with on the projects presented in this thesis. Thank you all for your support, feedback, and help in making the projects succeed. A huge thank you to all past and present colleagues at KMF for the enjoyable fika and lunch times. Further thanks to my current officemates (Elin, Quan, and Sofia) for the laughs and our birthday tradition.

My first six months in Sweden would not have been as easy and fun without Lea, Ahmad, and Louis. Thank you all for the wonderful trips and hikes around Sweden. I am also grateful to my friends (Krisztián and Rio) for sharing in the joys, frustrations, and 'keluh kesah' of our PhD journey in Sweden.

Although on the other side of the world, I wish to thank my family in Indonesia for always supporting my academic journey. I am also thankful to Niklas for being a good listener, encouraging me with my work, and providing meals during stressful times.

I would also like to thank the TOMCAT beamline at PSI for providing the beamtime. Finally, I gratefully acknowledge the generous funding from the Knut och Alice Foundation through the Wallenberg Wood Science Center, which enabled me to pursue my research and PhD without financial burden.

Last but not least, although I am studying rechargeable Zn-metal batteries, I should clarify that this doesn't mean I can magically fix your dead remote control.

References

- [1] A. Jannesar Niri, G. A. Poelzer, S. E. Zhang, J. Rosenkranz, M. Pettersson, and Y. Ghorbani, *Renewable and Sustainable Energy Reviews* vol. 191, p. 114 176, 2024, DOI: 10.1016/j.rser.2023.114176.
- [2] K. Hasan, N. Tom, and M. R. Yuce, *Batteries* vol. 9, p. 580, 2023, DOI: 10.3390/batteries9120580.
- [3] K. R. Ngoy, V. T. Lukong, K. O. Yoro, J. B. Makambo, N. C. Chukwuati, C. Ibegbulam, O. Eterigho-Ikelegbe, K. Ukoba, and T.-C. Jen, *Renewable and Sustainable Energy Reviews* vol. 223, p. 115 971, 2025, DOI: 10.1016/j.rser.2025.115971.
- [4] M. Iturrondobeitia, O. Akizu-Gardoki, O. Amondarain, R. Minguez, and E. Lizundia, *Advanced Sustainable Systems* vol. 6, p. 2 100 308, 2022, DOI: 10.1002/adsu.202100308.
- [5] G. N. Newton, L. R. Johnson, D. A. Walsh, B. J. Hwang, and H. Han, *ACS Sustainable Chemistry & Engineering* vol. 9, pp. 6507–6509, 2021, DOI: 10.1021/acssuschemeng.1c02909.
- [6] H. Ren, D. Mu, C. Wang, X. Yue, Z. Li, J. Du, L. Zhao, and M. K. Lim, *Computers & Industrial Engineering* vol. 188, p. 109 919, 2024, DOI: 10.1016/j.cie.2024.109919.
- [7] C. Bauer et al., *Nature Sustainability* vol. 5, pp. 176–178, 2022, DOI: 10.1038/s41893-022-00864-1.
- [8] P. J. Bugryniec, E. G. Resendiz, S. M. Nwophoke, S. Khanna, C. James, and S. F. Brown, *Journal of Energy Storage* vol. 87, p. 111 288, 2024, DOI: 10.1016/j.est.2024.111288.
- [9] E. Grignon, A. M. Battaglia, T. B. Schon, and D. S. Seferos, *iScience* vol. 25, p. 104 204, 2022, DOI: 10.1016/j.isci.2022.104204.
- [10] M. Karlsmo and P. Johansson, *Batteries & Supercaps* vol. 5, e202200306, 2022, DOI: 10.1002/batt.202200306.
- [11] X. Fan et al., *Transactions of Tianjin University* vol. 26, pp. 92–103, 2020, DOI: 10.1007/s12209-019-00231-w.
- [12] J. F. Parker, C. N. Chervin, I. R. Pala, M. Machler, M. F. Burz, J. W. Long, and D. R. Rolison, *Science* vol. 356, pp. 415–418, 2017, DOI: 10.1126/science.aak9991.

-
- [13] H. Au, M. Crespo-Ribadeneyra, and M.-M. Titirici, *One Earth* vol. 5, pp. 207–211, 2022, DOI: 10.1016/j.oneear.2022.02.014.
- [14] Y.-Y. Hsieh and H.-Y. Tuan, *Energy Storage Materials* vol. 68, p. 103 361, 2024, DOI: 10.1016/j.ensm.2024.103361.
- [15] J. Guo, J. L. Schaefer, and Y. Shao, *Energy Material Advances* vol. 5, p. 0112, 2024, DOI: 10.34133/energymatadv.0112.
- [16] M. R. Palacin et al., *Journal of Physics: Energy* vol. 6, p. 031 501, 2024, DOI: 10.1088/2515-7655/ad34fc.
- [17] A. Mahmood, Z. Bai, T. Wang, Y. Lei, S. Wang, B. Sun, H. Khan, K. Khan, K. Sun, and G. Wang, *Chemical Society Reviews* vol. 54, pp. 2369–2435, 2025, DOI: 10.1039/D4CS00929K.
- [18] M. Song, H. Tan, D. Chao, and H. J. Fan, *Advanced Functional Materials* vol. 28, p. 1 802 564, 2018, DOI: 10.1002/adfm.201802564.
- [19] Z. Ju, T. Zheng, B. Zhang, and G. Yu, *Chemical Society Reviews* vol. 53, pp. 8980–9028, 2024, DOI: 10.1039/D4CS00474D.
- [20] M. Fleischer, *Journal of Chemical Education* vol. 31, p. 446, 1954, DOI: 10.1021/ed031p446.
- [21] D. Chao, W. Zhou, F. Xie, C. Ye, H. Li, M. Jaroniec, and S.-Z. Qiao, *Science Advances* vol. 6, eaba4098, 2020, DOI: 10.1126/sciadv.aba4098.
- [22] A. Kim, Y. Park, J. Choi, S.-H. Yu, and K. W. Nam, *ACS Applied Energy Materials* vol. 8, pp. 6806–6828, 2025, DOI: 10.1021/acsaem.5c00602.
- [23] A. Duan, S. Luo, and W. Sun, *Chinese Chemical Letters* vol. 35, p. 108 337, 2024, DOI: 10.1016/j.cclet.2023.108337.
- [24] R. Deng, Z. He, F. Chu, J. Lei, Y. Cheng, Y. Zhou, and F. Wu, *Nature Communications* vol. 14, p. 4981, 2023, DOI: 10.1038/s41467-023-40462-z.
- [25] M. Wang, Y. Meng, X. Li, J. Qi, A. Li, and S. Huang, *Chemical Engineering Journal* vol. 507, p. 160 615, 2025, DOI: 10.1016/j.cej.2025.160615.
- [26] M. Al-Abbasi et al., *Carbon Neutralization* vol. 3, pp. 108–141, 2024, DOI: 10.1002/cn12.109.
- [27] A. Klein, M. Sadd, N. Mozhzhukhina, M. Olsson, L. Broche, S. Xiong, and A. Matic, *Batteries & Supercaps*, e202400070, 2024, DOI: 10.1002/batt.202400070.
- [28] T. Wang, C. Li, X. Xie, B. Lu, Z. He, S. Liang, and J. Zhou, *ACS Nano* vol. 14, pp. 16 321–16 347, 2020, DOI: 10.1021/acsnano.0c07041.
-

-
- [29] E. R. Cooper, M. Li, I. Gentle, Q. Xia, and R. Knibbe, *Angewandte Chemie International Edition* vol. 62, e202309247, 2023, DOI: 10.1002/anie.202309247.
- [30] F. Omenya, M. Paiss, X. Li, and D. Reed, *ACS Energy Letters* vol. 8, pp. 2707–2710, 2023, DOI: 10.1021/acseenergylett.3c00660.
- [31] X. Guo and G. He, *Journal of Materials Chemistry A* vol. 11, pp. 11 987–12 001, 2023, DOI: 10.1039/D3TA01904G.
- [32] S. Mallick and C. R. Raj, *ChemSusChem* vol. 14, pp. 1987–2022, 2021, DOI: 10.1002/cssc.202100299.
- [33] T. Yamamoto and T. Shoji, *Inorganica Chimica Acta* vol. 117, pp. L27–L28, 1986, DOI: 10.1016/S0020-1693(00)82175-1.
- [34] C. Xu, B. Li, H. Du, and F. Kang, *Angewandte Chemie International Edition* vol. 51, pp. 933–935, 2012, DOI: 10.1002/anie.201106307.
- [35] N. Borchers, S. Clark, B. Horstmann, K. Jayasayee, M. Juel, and P. Stevens, *Journal of Power Sources* vol. 484, p. 229 309, 2021, DOI: 10.1016/j.jpowsour.2020.229309.
- [36] J. Shin, J. Lee, Y. Park, and J. W. Choi, *Chemical Science* vol. 11, pp. 2028–2044, 2020, DOI: 10.1039/D0SC00022A.
- [37] Y. Gong, B. Wang, H. Ren, D. Li, D. Wang, H. Liu, and S. Dou, *Nano-Micro Letters* vol. 15, p. 208, 2023, DOI: 10.1007/s40820-023-01177-4.
- [38] L. Miao, W. Jia, and L. Jiao, *Chemical Science* vol. 15, pp. 18 227–18 238, 2024, DOI: 10.1039/D4SC06319H.
- [39] Z. Hu et al., *Nano-Micro Letters* vol. 15, p. 171, 2023, DOI: 10.1007/s40820-023-01136-z.
- [40] Z. Yi, G. Chen, F. Hou, L. Wang, and J. Liang, *Advanced Energy Materials* vol. 11, p. 2 003 065, 2021, DOI: 10.1002/aenm.202003065.
- [41] W. Du, E. H. Ang, Y. Yang, Y. Zhang, M. Ye, and C. C. Li, *Energy & Environmental Science* vol. 13, pp. 3330–3360, 2020, DOI: 10.1039/D0EE02079F.
- [42] A. A and S. Bag, *Chemistry – An Asian Journal* vol. 20, e70004, 2025, DOI: 10.1002/asia.202500120.
- [43] Y. Zhang, X. Zheng, N. Wang, W.-H. Lai, Y. Liu, S.-L. Chou, H.-K. Liu, S.-X. Dou, and Y.-X. Wang, *Chemical Science* vol. 13, pp. 14 246–14 263, 2022, DOI: 10.1039/D2SC04945G.
- [44] Z. Cao, P. Zhuang, X. Zhang, M. Ye, J. Shen, and P. M. Ajayan, *Advanced Energy Materials* vol. 10, p. 2 001 599, 2020, DOI: 10.1002/aenm.202001599.
-

-
- [45] Y. Zhu, G. Liang, X. Cui, X. Liu, H. Zhong, C. Zhi, and Y. Yang, *Energy & Environmental Science* vol. 17, pp. 369–385, 2024, DOI: 10.1039/D3EE03584K.
- [46] H. Li, R. Zhao, W. Zhou, L. Wang, W. Li, D. Zhao, and D. Chao, *JACS Au* vol. 3, pp. 2107–2116, 2023, DOI: 10.1021/jacsau.3c00292.
- [47] Z. Li and A. W. Robertson, *Battery Energy* vol. 2, p. 20 220 029, 2023, DOI: 10.1002/bte2.20220029.
- [48] X. Tian, Y. Sun, H. Li, X. Duan, Q. Zhao, and T. Ma, *Advanced Energy Materials* vol. 15, p. 2 403 995, 2025, DOI: 10.1002/aenm.202403995.
- [49] Q. Cao, Y. Gao, J. Pu, A. M. Elshahawy, and C. Guan, *SmartMat* vol. 5, e1194, 2024, DOI: 10.1002/smm2.1194.
- [50] H. Liu, Y. Zhang, C. Wang, J. N. Glazer, Z. Shan, and N. Liu, *ACS Applied Materials & Interfaces* vol. 13, pp. 32 930–32 936, 2021, DOI: 10.1021/acsami.1c06131.
- [51] Z. Cai et al., *Angewandte Chemie International Edition* vol. 61, e202116560, 2022, DOI: 10.1002/anie.202116560.
- [52] Y. Zhang, G. Yang, M. L. Lehmann, C. Wu, L. Zhao, T. Saito, Y. Liang, J. Nanda, and Y. Yao, *Nano Letters* vol. 21, pp. 10 446–10 452, 2021, DOI: 10.1021/acs.nanolett.1c03792.
- [53] J. Zhang, M. Shi, H. Gao, X. Ren, J. Cao, G. Li, A. Wang, and C. Liu, *Chemical Engineering Journal* vol. 491, p. 152 050, 2024, DOI: 10.1016/j.cej.2024.152050.
- [54] H. Yan, S. Li, J. Zhong, and B. Li, *Nano-Micro Letters* vol. 16, p. 15, 2024, DOI: 10.1007/s40820-023-01227-x.
- [55] R. Qi, W. Tang, Y. Shi, K. Teng, Y. Deng, L. Zhang, J. Zhang, and R. Liu, *Advanced Functional Materials* vol. 33, p. 2 306 052, 2023, DOI: 10.1002/adfm.202306052.
- [56] C. Xu, T. Jiang, C. Zhu, W. Gou, K. Zang, J. Jia, R. Zhang, X. Wang, G. Li, and Q. Fan, *ACS Applied Materials & Interfaces* vol. 17, pp. 41 379–41 402, 2025, DOI: 10.1021/acsami.5c01165.
- [57] Y. Shang and D. Kundu, *Batteries & Supercaps* vol. 5, e202100394, 2022, DOI: 10.1002/batt.202100394.
- [58] L. Yan, Q. Zhai, S. Zhang, Z. Li, Q. Kang, X. Gao, C. Jin, T. Liu, T. Ma, and Z. Lin, *Advanced Energy Materials* vol. 14, p. 2 401 328, 2024, DOI: 10.1002/aenm.202401328.
- [59] M. Lee, H. Lee, J. Han, C. Kim, and H. Lee, *Current Opinion in Electrochemistry* vol. 47, p. 101 571, 2024, DOI: 10.1016/j.coelec.2024.101571.
-

-
- [60] S. Konwar et al., *Materials Today Communications*, p. 113755, 2025, DOI: 10.1016/j.mtcomm.2025.113755.
- [61] W. Huang, L. Wang, Q. Zhu, P. Zhang, X. Pu, and L. Gao, *Materials Today Communications* vol. 33, p. 104576, 2022, DOI: 10.1016/j.mtcomm.2022.104576.
- [62] L. Wang, S. Zhou, K. Yang, W. Huang, S. Ogata, L. Gao, and X. Pu, *Advanced Science* vol. 11, p. 2307667, 2024, DOI: 10.1002/advs.202307667.
- [63] F. Yang et al., *Advanced Materials* vol. 34, p. 2206754, 2022, DOI: 10.1002/adma.202206754.
- [64] M. Naguib, O. Mashtalir, J. Carle, V. Presser, J. Lu, L. Hultman, Y. Gogotsi, and M. W. Barsoum, *ACS Nano* vol. 6, pp. 1322–1331, 2012, DOI: 10.1021/nn204153h.
- [65] Z. Wang, S. Hu, D. Wang, J. Huang, J. Qi, H. Liu, X. Li, C. Han, and H.-M. Cheng, *Advanced Functional Materials* vol. 35, p. 2502186, 2025, DOI: 10.1002/adfm.202502186.
- [66] Z. Cai, J. Wang, and Y. Sun, *eScience* vol. 3, p. 100093, 2023, DOI: 10.1016/j.esci.2023.100093.
- [67] C. Fan, W. Meng, and J. Ye, *Journal of Energy Chemistry* vol. 93, pp. 79–110, 2024, DOI: 10.1016/j.jechem.2023.12.054.
- [68] X. Zhang, J.-P. Hu, N. Fu, W.-B. Zhou, B. Liu, Q. Deng, and X.-W. Wu, *InfoMat* vol. 4, e12306, 2022, DOI: 10.1002/inf2.12306.
- [69] A. Li, J. Li, Y. He, and M. Wu, *Journal of Energy Chemistry* vol. 83, pp. 209–228, 2023, DOI: 10.1016/j.jechem.2023.04.006.
- [70] X. Zheng, T. Ahmad, and W. Chen, *Energy Storage Materials* vol. 39, pp. 365–394, 2021, DOI: 10.1016/j.ensm.2021.04.027.
- [71] H. Yoon, C. Choi, S. Hong, M. Afiandika, A. Matic, T. G. Yun, and B. Hwang, *International Journal of Energy Research* vol. 2025, 2025, DOI: 10.1155/er/1405163.
- [72] S. Hong, Z. Choi, B. Hwang, and A. Matic, *ACS Energy Letters* vol. 9, pp. 5421–5433, 2024, DOI: 10.1021/acsenergylett.4c02191.
- [73] Q. Nian et al., *Nature Communications* vol. 15, p. 4303, 2024, DOI: 10.1038/s41467-024-48444-5.
- [74] J. Zheng et al., *Science* vol. 366, pp. 645–648, 2019, DOI: 10.1126/science.aax6873.
- [75] X. Jiao, Y. Wang, O. O. Kapitanova, X. Xu, V. S. Volkov, Y. Liu, Z. Song, A. Matic, and S. Xiong, *Energy Storage Materials* vol. 61, p. 102916, 2023, DOI: 10.1016/j.ensm.2023.102916.
-

-
- [76] Y. Liu et al., *Advanced Science* vol. 8, p. 2003301, 2021, DOI: 10.1002/adv.202003301.
- [77] Y. Ran, F. Dong, S. Sun, and Y. Lei, *Advanced Energy Materials*, p. 2406139, 2025, DOI: 10.1002/aenm.202406139.
- [78] J. Zheng and L. A. Archer, *Science Advances* vol. 7, eabe0219, 2021, DOI: 10.1126/sciadv.abe0219.
- [79] T. Foroozan, V. Yurkiv, S. Sharifi-Asl, R. Rojaee, F. Mashayek, and R. Shahbazian-Yassar, *ACS Applied Materials & Interfaces* vol. 11, pp. 44077–44089, 2019, DOI: 10.1021/acsmi.9b13174.
- [80] J. Zheng et al., *Science* vol. 366, pp. 645–648, 2019, DOI: 10.1126/science.aax6873.
- [81] L. Hong, L.-Y. Wang, Y. Wang, X. Wu, W. Huang, Y. Zhou, K.-X. Wang, and J.-S. Chen, *Advanced Science* vol. 9, p. 2104866, 2022, DOI: 10.1002/adv.202104866.
- [82] Y. Zhang, S. Yang, Y.-J. Zhu, D. Li, L. Cheng, H. Li, and Z. Wang, *Journal of Colloid and Interface Science* vol. 656, pp. 566–576, 2024, DOI: 10.1016/j.jcis.2023.11.132.
- [83] Z. He et al., *Energy Storage Materials* vol. 74, p. 103886, 2025, DOI: 10.1016/j.ensm.2024.103886.
- [84] P. Chen et al., *Advanced Functional Materials* vol. 34, 2024, DOI: 10.1002/adfm.202409368.
- [85] Z. Zhang et al., *Green Energy & Environment*, 2025, DOI: 10.1016/j.gee.2025.03.010.
- [86] Y. Li, X. Peng, X. Li, H. Duan, S. Xie, L. Dong, and F. Kang, *Advanced Materials* vol. 35, 2023, DOI: 10.1002/adma.202300019.
- [87] Y. Luo, Y. Yang, Y. Tao, D. Huang, B. Huang, and H. Chen, *ACS Applied Energy Materials* vol. 4, pp. 14599–14607, 2021, DOI: 10.1021/acsaem.1c03223.
- [88] D. Qiu, B. Li, C. Zhao, J. Dang, G. Chen, H. Qiu, and H. Miao, *Energy Storage Materials* vol. 61, p. 102903, 2023, DOI: 10.1016/j.ensm.2023.102903.
- [89] A. J. Sellathurai, M. Khademi, B. X. Zhang, M. Al-Hamdani, and D. P. J. Barz, *Langmuir* vol. 41, pp. 19204–19217, 2025, DOI: 10.1021/acs.langmuir.5c01550.
- [90] N. Wang, H. Wan, J. Duan, X. Wang, L. Tao, J. Zhang, and H. Wang, *Materials Today Advances* vol. 11, p. 100149, 2021, DOI: 10.1016/j.mtadv.2021.100149.
-

-
- [91] J. Ming, J. Guo, C. Xia, W. Wang, and H. N. Alshareef, *Materials Science and Engineering: R: Reports* vol. 135, pp. 58–84, 2019, DOI: 10.1016/j.mser.2018.10.002.
- [92] H. Yan, X. Zhang, Z. Yang, M. Xia, C. Xu, Y. Liu, H. Yu, L. Zhang, and J. Shu, *Coordination Chemistry Reviews* vol. 452, p. 214297, 2022, DOI: 10.1016/j.ccr.2021.214297.
- [93] J. Zhou, L. Shan, Z. Wu, X. Guo, G. Fang, and S. Liang, *Chemical Communications* vol. 54, pp. 4457–4460, 2018, DOI: 10.1039/C8CC02250J.
- [94] W. Deng, G. Li, and X. Wang, *Advanced Functional Materials* vol. 34, p. 2405012, 2024, DOI: 10.1002/adfm.202405012.
- [95] X. Liu, L. Sun, Z. Zhao, and Q. Lu, *Journal of Energy Storage* vol. 89, p. 111822, 2024, DOI: 10.1016/j.est.2024.111822.
- [96] Y. Wang, Z. Wang, F. Yang, S. Liu, S. Zhang, J. Mao, and Z. Guo, *Small* vol. 18, p. 2107033, 2022, DOI: 10.1002/smll.202107033.
- [97] F. Wang, O. Borodin, T. Gao, X. Fan, W. Sun, F. Han, A. Faraone, J. A. Dura, K. Xu, and C. Wang, *Nature Materials* vol. 17, pp. 543–549, 2018, DOI: 10.1038/s41563-018-0063-z.
- [98] X. Guo, S. Zhang, H. Hong, S. Wang, J. Zhu, and C. Zhi, *iScience* vol. 28, p. 111751, 2025, DOI: 10.1016/j.isci.2025.111751.
- [99] Y. Zhang, X. Fu, Y. Ding, Y. Liu, Y. Zhao, and S. Jiao, *Small* vol. 20, p. 2311407, 2024, DOI: 10.1002/smll.202311407.
- [100] L. Cao, D. Li, E. Hu, J. Xu, T. Deng, L. Ma, Y. Wang, X.-Q. Yang, and C. Wang, *Journal of the American Chemical Society* vol. 142, pp. 21404–21409, 2020, DOI: 10.1021/jacs.0c09794.
- [101] Y. Lv, Y. Xiao, L. Ma, C. Zhi, and S. Chen, *Advanced Materials* vol. 34, p. 2106409, 2022, DOI: 10.1002/adma.202106409.
- [102] Z. Hou, X. Zhang, X. Li, Y. Zhu, J. Liang, and Y. Qian, *Journal of Materials Chemistry A* vol. 5, pp. 730–738, 2017, DOI: 10.1039/C6TA08736A.
- [103] D. Wang, Q. Li, Y. Zhao, H. Hong, H. Li, Z. Huang, G. Liang, Q. Yang, and C. Zhi, *Advanced Energy Materials* vol. 12, p. 2102707, 2022, DOI: 10.1002/aenm.202102707.
- [104] S.-D. Han, N. N. Rajput, X. Qu, B. Pan, M. He, M. S. Ferrandon, C. Liao, K. A. Persson, and A. K. Burrell, *ACS Applied Materials & Interfaces* vol. 8, pp. 3021–3031, 2016, DOI: 10.1021/acsami.5b10024.
- [105] F. Cheng et al., *Energy Storage Materials* vol. 74, p. 103933, 2025, DOI: 10.1016/j.ensm.2024.103933.
-

-
- [106] J. Tang, Z. Dai, C. Yang, R. Chanajaree, M. Okhawilai, P. Pattananuwat, S. Rajendran, X. Zhang, and J. Qin, *Advanced Functional Materials*, e15911, 2025, DOI: 10.1002/adfm.202515911.
- [107] H. Qiu, X. Du, J. Zhao, Y. Wang, J. Ju, Z. Chen, Z. Hu, D. Yan, X. Zhou, and G. Cui, *Nature Communications* vol. 10, p. 5374, 2019, DOI: 10.1038/s41467-019-13436-3.
- [108] S. Islam, M. H. Alfaruqi, D. Y. Putro, V. Soundharrajan, B. Sambandam, J. Jo, S. Park, S. Lee, V. Mathew, and J. Kim, *Journal of Materials Chemistry A* vol. 7, pp. 20 335–20 347, 2019, DOI: 10.1039/C9TA05767F.
- [109] R. Deivanayagam and R. Shahbazian-Yassar, *Batteries & Supercaps* vol. 4, pp. 596–606, 2021, DOI: 10.1002/batt.202000221.
- [110] A. Mathew, M. J. Lacey, and D. Brandell, *Journal of Power Sources Advances* vol. 11, p. 100 071, 2021, DOI: 10.1016/j.powera.2021.100071.
- [111] G. Hernández, I. L. Johansson, A. Mathew, C. Sångeland, D. Brandell, and J. Mindemark, *Journal of The Electrochemical Society* vol. 168, p. 100 523, 2021, DOI: 10.1149/1945-7111/ac2d8b.
- [112] L. Ma, M. A. Schroeder, O. Borodin, T. P. Pollard, M. S. Ding, C. Wang, and K. Xu, *Nature Energy* vol. 5, pp. 743–749, 2020, DOI: 10.1038/s41560-020-0674-x.
- [113] L. Ma et al., *Energy & Environmental Materials* vol. 3, pp. 516–521, 2020, DOI: 10.1002/eem2.12077.
- [114] C. Cao, M. F. Toney, T.-K. Sham, R. Harder, P. R. Shearing, X. Xiao, and J. Wang, *Materials Today* vol. 34, pp. 132–147, 2020, DOI: 10.1016/j.mattod.2019.08.011.
- [115] B.-K. Cho, S.-Y. Jung, S.-J. Park, J.-H. Hyun, and S.-H. Yu, *ACS Energy Letters* vol. 9, pp. 4068–4092, 2024, DOI: 10.1021/acsenerylett.4c01098.
- [116] M. Sadd, S. Xiong, J. R. Bowen, F. Marone, and A. Matic, *Nature Communications* vol. 14, p. 854, 2023, DOI: 10.1038/s41467-023-36568-z.
- [117] Q. Wu, E. D. Esping, M. Afiandika, S. Xiong, and A. Matic, *eScience*, p. 100 429, 2025, DOI: 10.1016/j.esci.2025.100429.
- [118] S. Kunze, C. Nam, H. Kim, J. Chung, E. Hong, J. Song, H. Choi, and J. Lim, *Bulletin of the Korean Chemical Society* vol. 46, pp. 360–380, 2025, DOI: 10.1002/bkcs.70009.
- [119] F. Tang et al., *Small Methods* vol. 5, p. 2100 557, 2021, DOI: 10.1002/smt.202100557.
-

-
- [120] P. J. Withers, C. Bouman, S. Carmignato, V. Cnudde, D. Grimaldi, C. K. Hagen, E. Maire, M. Manley, A. Du Plessis, and S. R. Stock, *Nature Reviews Methods Primers* vol. 1, p. 18, 2021, DOI: 10.1038/s43586-021-00015-4.
- [121] K. Vernon-Parry, *III-Vs Review* vol. 13, pp. 40–44, 2000, DOI: 10.1016/S0961-1290(00)80006-X.
- [122] W. Zhou, R. Apkarian, Z. L. Wang, and D. Joy, “Fundamentals of Scanning Electron Microscopy (SEM),” en, in *Scanning Microscopy for Nanotechnology*, W. Zhou and Z. L. Wang, Eds., New York, NY: Springer New York, 2006, pp. 1–40, ISBN: 978-0-387-33325-0 978-0-387-39620-0.
- [123] Z. Liu et al., *Chemical Reviews* vol. 125, pp. 5228–5281, 2025, DOI: 10.1021/acs.chemrev.4c00831.
- [124] V. A. J. Jaques, E. Zikmundová, J. Holas, T. Zikmund, J. Kaiser, and K. Holcová, *Scientific Reports* vol. 12, p. 19650, 2022, DOI: 10.1038/s41598-022-21882-1.
- [125] H. Williams, *Physics Education* vol. 56, p. 055034, 2021, DOI: 10.1088/1361-6552/ac1503.
- [126] Y. Deng, S. Dong, Z. Li, H. Jiang, X. Zhang, and X. Ji, *Small Methods* vol. 2, p. 1700332, 2018, DOI: 10.1002/smtd.201700332.
- [127] M. Weiling, F. Pfeiffer, and M. Baghernejad, *Advanced Energy Materials* vol. 12, p. 2202504, 2022, DOI: 10.1002/aenm.202202504.
- [128] G. Agrawal and S. K. Samal, *ACS Biomaterials Science & Engineering* vol. 4, pp. 1285–1299, 2018, DOI: 10.1021/acsbiomaterials.8b00258.
- [129] A. Weber, B. Hoplight, R. Ogilvie, C. Muro, S. R. Khandasammy, L. Pérez-Almodóvar, S. Sears, and I. K. Lednev, *Analytical Chemistry* vol. 95, pp. 167–205, 2023, DOI: 10.1021/acs.analchem.2c05094.
- [130] S. Lee, I. Kang, J. Kim, S. H. Kim, K. Kang, and J. Hong, *Journal of Power Sources* vol. 472, p. 228334, 2020, DOI: 10.1016/j.jpowsour.2020.228334.
- [131] J. Zheng, T. Tang, Q. Zhao, X. Liu, Y. Deng, and L. A. Archer, *ACS Energy Letters* vol. 4, pp. 1349–1355, 2019, DOI: 10.1021/acsenenergylett.9b00750.
- [132] Z. Wu, Y. Li, and J. Liu, *Small Methods* vol. 8, p. 2300660, 2024, DOI: 10.1002/smtd.202300660.
- [133] Z. Wu, Y. Wang, and C. Zhi, *Joule* vol. 8, pp. 2442–2448, 2024, DOI: 10.1016/j.joule.2024.07.023.
-

- [134] G. Hao, X. Tian, X. Chen, Y. Dong, C. Hao, and C. Li, *Materials Today Chemistry* vol. 38, p. 102 059, 2024, DOI: 10.1016/j.mtchem.2024.102059.
- [135] O. S. Wostoupal, X. Wang, Q. Liu, T. Xu, and Z. Zhang, *Journal of The Electrochemical Society* vol. 172, p. 060 515, 2025, DOI: 10.1149/1945-7111/addef1.
- [136] M. Cao, F. Bu, X. Liu, C. H. Ng, and C. Guan, *Advanced Energy Materials* vol. 15, p. 2 502 540, 2025, DOI: 10.1002/aenm.202502540.
- [137] X. Guo, L. Liu, J. Wu, J. Fan, and Y. Wu, *RSC Advances* vol. 8, pp. 4214–4220, 2018, DOI: 10.1039/c7ra09894d.
- [138] D. Lei et al., *Advanced Energy Materials* vol. 14, p. 2 403 030, 2024, DOI: 10.1002/aenm.202403030.
- [139] W. Kao-ian, A. A. Mohamad, W.-R. Liu, R. Pornprasertsuk, S. Siwamogsatham, and S. Kheawhom, *Batteries & Supercaps* vol. 5, e202100361, 2022, DOI: 10.1002/batt.202100361.
- [140] H. Li, Z. Chen, L. Zheng, J. Wang, H. Adenusi, S. Passerini, and H. Zhang, *Small Methods* vol. 8, p. 2 300 554, 2024, DOI: 10.1002/smt.202300554.